Check for updates

Meteorological Applications

RMetS Royal Meteorological Society

RESEARCH ARTICLE OPEN ACCESS

Harnessing Subseasonal-to-Seasonal Predictability for Wind Energy in Kenya

Gibbon Innocent Tirivanhu Masukwedza[1,2,3] | Linda C. Hirons[1,3] | Steven J. Woolnough[1,3] | Cohen Ang'u[4] | Hannah C. Bloomfield[5] | Caroline M. Wainwright[6] | David James Brayshaw[3] | Eve de Vincelles[7] | Wilson Gitau[4] | Joseph Mutemi[4] | Willis Owino Ochieng[8] | Daniel Olago[4] | Christopher Oludhe[4]

[1]National Centre for Atmospheric Science, University of Reading, Reading, UK | [2]Department of Geography, University of Sussex, Brighton, UK | [3]Department of Meteorology, University of Reading, Reading, UK | [4]Department of Earth & Climate Sciences, University of Nairobi, Nairobi, Kenya | [5]School of Engineering, Newcastle University, Newcastle upon Tyne, UK | [6]School of Earth & Environment, University of Leeds, Leeds, UK | [7]Institut National des Sciences Appliquées de Lyon, Département Génie Énergétique et Environnement, Villeurbanne, France | [8]Kenya Electricity Generating Company PLC, KenGen, Nairobi, Kenya

Correspondence: Gibbon Innocent Tirivanhu Masukwedza (g.t.masukwedza@reading.ac)

Received: 26 February 2026 | **Revised:** 18 May 2026 | **Accepted:** 7 July 2026

Keywords: East Africa | El Niño–Southern Oscillation (ENSO) | Energy climate information and services | Indian Ocean Dipole (IOD) | Kenya | Madden–Julian Oscillation (MJO) | Subseasonal-to-seasonal (S2S) predictability | wind energy | wind power

ABSTRACT

Understanding how climate variability influences wind-power resources is critical for energy security, particularly in countries such as Kenya where reliance on weather-sensitive generation is increasing. Using ERA5 reanalysis, climate-mode indices, site observations where available and modelled wind-power potential, we quantify how three major tropical climate modes relevant to subseasonal-to-seasonal (S2S) wind-power variability, the Madden–Julian Oscillation (MJO), El Niño–Southern Oscillation (ENSO) and Indian Ocean Dipole (IOD), influence Kenya's wind-energy system. Results show that MJO Phases 2–4 generally suppress wind-energy potential across Kenya, while Phases 6–8 enhance it. ENSO influences are weaker and more seasonally selective, with El Niño favouring suppressed wind-energy potential during October–November–December and La Niña favouring enhancement during April–May–June. The IOD imprint is strongest in October–November–December, when positive IOD conditions weaken wind-energy potential across key inland regions and negative IOD conditions strengthen it. Using a perfect-forecast framework that assumes known MJO, ENSO and IOD states, with forecast skill evaluated through leave-one-out cross-validation, we quantify the potential value of climate-mode information for wind-power prediction. We show that conditioning on the MJO provides the largest single-mode improvements in deterministic and probabilistic wind-power forecast skill relative to monthly climatology. Conditioning on ENSO and the IOD yields smaller, season-dependent skill gains, with the strongest improvements occurring in October–November–December. Combined MJO–ENSO–IOD conditioning gives the largest overall skill improvement. Taken together, these results identify a clear hierarchy of predictability: MJO information provides the strongest subseasonal contribution to wind-power prediction, while ENSO and IOD provide broader seasonal context and smaller refinements. This hierarchy supports the development of climate-mode-informed "windows of risk and opportunity" that translate S2S climate information into practical services for anticipatory, risk-informed wind-energy operations and planning in Kenya, with potential relevance for wider East Africa.

This is an open access article under the terms of the Creative Commons Attribution License, which permits use, distribution and reproduction in any medium, provided the original work is properly cited.

© 2026 The Author(s). *Meteorological Applications* published by John Wiley & Sons Ltd on behalf of Royal Meteorological Society.

1 | Introduction

The Sustainable Development Goals (SDGs), particularly SDG 7 on clean and affordable energy and SDG 13 on climate action (UNDP 2025), have accelerated the global shift towards low-carbon energy systems. In East Africa, this transition is supported by the existence of abundant renewable resources and coordinated regional planning frameworks, such as the Africa Clean Energy Corridor initiative (Saadi et al. 2015). Renewable energy deployment in the region has expanded steadily over the past decade, with hydropower increasingly complemented by solar and wind technologies (IRENA 2025). In Kenya, this expansion is exemplified by operational wind farms at Lake Turkana (LTWP 2019), Ngong Hills (KenGen 2025), Kipeto (The Wind Power 2025) and Kilifi (Global Data 2024), with additional proposed or pipeline developments in counties such as Laikipia, Meru, Narok Plains, Nyandarua, Nyeri and Samburu, which have been earmarked for high wind-power potential (Rotich et al. 2024). Collectively, these developments have accelerated the electricity-sector shift from fossil fuels to renewable generation, with renewables supplying nearly 90% of total power generation as of 2023 (Fernández 2025).

Large-scale climate modes influence East African weather across intraseasonal to interannual timescales. Among these, the Madden–Julian Oscillation (MJO) is a major source of intraseasonal variability, modulating convection and atmospheric circulation across the region, with associated effects on rainfall (Pohl and Camberlin 2006a, 2006b; Berhane and Zaitchik 2014; Nicholson 2017; Zaitchik 2017; Kilavi et al. 2018; Finney et al. 2019; Vashisht and Zaitchik 2022; Maybee et al. 2022; Talib et al. 2023). MJO phases 2–4 are generally associated with enhanced rainfall, whereas phases 6–8 tend to suppress rainfall during both the long and short rainy seasons (MacLeod et al. 2021; Talib et al. 2023; Gudoshava et al. 2024; Mwangi et al. 2024). The East African rainfall response to the MJO may also be modulated by the Quasi-Biennial Oscillation, indicating a possible interaction between intraseasonal tropical variability and stratospheric circulation (Berihu et al. 2026).

At seasonal-to-interannual timescales, El Niño–Southern Oscillation (ENSO) and the Indian Ocean Dipole (IOD) have major influences on East African rainfall and atmospheric circulation variability (Nicholson 2017; Mbigi and Xiao 2021; Bloomfield et al. 2022; Vashisht and Zaitchik 2022; Sun et al. 2022; Palmer et al. 2023; Roy and Troccoli 2024). El Niño and positive IOD conditions are generally associated with wetter conditions, whereas La Niña and negative IOD conditions tend to favour drier conditions, with the IOD exerting particularly strong control over the October–November–December short rains (Saji et al. 1999; Hirons and Turner 2018; Lüdecke et al. 2021).

These large-scale climate modes also influence winds over Kenya partly through their interactions with regional circulation systems operating at different atmospheric levels. The seasonal migration of the Intertropical Convergence Zone shapes the distribution of convection and rainfall across East Africa (Roy and Troccoli 2024; Yao et al. 2026), while the upper-level Tropical Easterly Jet influences regional circulation and moisture transport (Yao et al. 2026). At lower levels, the Turkana Jet is a prominent wind feature over northern Kenya with direct relevance for the Lake Turkana wind-resource region (Nicholson 2015; Talib et al. 2023). Kenya's complex topography further modulates these atmospheric circulation patterns and contributes to strong spatial variability in near-surface airflow (Nicholson 2017).

Together, these large-scale and regional circulation processes influence wind conditions across Kenya. Wetter seasons are typically associated with enhanced westerly wind anomalies that increase moisture convergence and ascent, whereas drier seasons are associated with enhanced easterly winds, reduced moisture inflow and subsidence that suppress convection (Nicholson 2017; Palmer et al. 2023). Consequently, even with the rapid growth in renewable-energy capacity, wind-power generation in Kenya remains sensitive to climate variability operating across intraseasonal to interannual timescales.

Despite substantial advances in understanding East African climate variability and extremes, much of this work has been framed through impact on agriculture, water resources and disaster risk (e.g., Nicholson 2017; Kilavi et al. 2018; MacLeod et al. 2021; Vashisht and Zaitchik 2022; Ochieng et al. 2022; Talib et al. 2023; Mwangi et al. 2024; Roy and Troccoli 2024; Afolayan and Mekonnen 2026), far less is known about how these climate modes modulate near-surface wind variability, with implications for wind-power generation and broader energy-system performance. For Kenya, previous work examining the impact of climate modes on solar photovoltaic and wind-power potential has largely focused on seasonal-to-interannual variability, particularly ENSO-related influences (e.g., Bloomfield et al. 2022), with the roles of intraseasonal drivers, notably the MJO and the IOD on intraseasonal-to-seasonal timescales remaining largely unexplored.

This gap is important because the intraseasonal-to-seasonal window, commonly termed the subseasonal-to-seasonal (S2S) timescale (Vitart and Robertson 2018), spans lead times from roughly 2 weeks to a season, a period particularly relevant for wind-energy planning. Forecasts at these lead times can identify periods of increased likelihood of low generation, high wind-power opportunity or anomalous wind conditions relevant to maintenance scheduling, reserve planning, dispatch decisions and grid balancing (White et al. 2022). Such information extends operational awareness beyond the lead times typically covered by deterministic weather forecasts and can support anticipatory planning for weather-sensitive renewable-energy systems. For context, the MJO is predictable with reasonable predictability skill at lead times of up to ~1 month (Kim et al. 2025; Wang et al. 2025), while ENSO and the IOD exhibit reasonable predictability skill of several months (~6–8 months; Chen et al. 2023; Ratnam et al. 2025). This combination of physical relevance and forecastability makes these modes plausible sources of climate information for anticipating wind-power variability in Kenya.

Building on this background, this study examines how these three major modes of S2S climate variability (the MJO, ENSO and IOD—Pohl et al. 2005; Mbigi and Xiao 2021; Palmer et al. 2023) modulate wind-power potential in Kenya. We focus on three central questions:

14698080, 2026, 4, Downloaded from https://rmets.onlinelibrary.wiley.com/doi/10.1002/met.70221 by NICE, National Institute for Health and Care Excellence, Wiley Online Library on [06/10/2026]. See the Terms and Conditions (https://onlinelibrary.wiley.com/terms-and-conditions) on Wiley Online Library for rules of use; OA articles are governed by the applicable Creative Commons License

i. How do these climate modes modulate wind speed and wind-power potential across Kenya, both spatially and at operational wind-farm sites?

ii. Can these climate modes provide useful predictability of wind-power variability on S2S timescales?

iii. What are the potential implications of any such predictability for wind-energy forecasting and operational decision-making in Kenya?

By clarifying how MJO, ENSO and IOD shape wind-energy variability across Kenya, this study provides an evidence base for impact-based forecasting (IbF) and climate information services that translate S2S predictability into actionable guidance on periods of elevated risk or opportunity for wind-energy generation, with potential application across the wider East African region.

2 | Study Area, Data and Methods

2.1 | Study Area and Wind-Farm Sites

This study focuses on Kenya, located in East Africa near the equator (approximately 5.0° N–4.7° S and 33.9° E–41.9° E), as shown in the Africa-wide panel of Figure 1 (left). The country encompasses a diverse range of topographic environments, including the Rift Valley highlands, extensive interior plains and a southeastern coastal margin along the western Indian Ocean (Figure 1, right).

Within this broader landscape, this study examines four major wind-farm sites in Kenya: Lake Turkana, Ngong Hills, Kipeto and Kilifi (approximate locations indicated in Figure 1, right), which together represent the country's key wind-power assets. The Lake Turkana Wind Farm, located in northern Kenya (≈36.7° E–36.9° E, 2.4° N–2.8° N), is the largest wind-farm project in Africa (Rotich et al. 2024), with an installed capacity of 310 megawatts (MW) (Hashimshony Yaffe and Segal-Klein 2023), contributing approximately one-fifth of Kenya's total installed electricity-generation capacity (LTWP 2019). The site lies within a region characterised by strong, topographically channelled winds associated with the Turkana Jet, which provides persistently high wind speeds throughout much of the year (LTWP 2009).

The Ngong Hills Wind Farm is situated in southern Kenya (≈36.5° E–36.75° E, 1.50° S–1.25° S) along the eastern escarpment of the Rift Valley and has an installed capacity of approximately 25 MW (KenGen 2025). Nearby, the Kipeto Wind Farm (≈36.6° E–36.9° E, 1.9° S–1.6° S) contributes around 100 MW to the national grid (The Wind Power 2025). Both sites are located in complex terrain, where steep topography strongly influences wind flow, resulting in enhanced spatial and temporal wind variability.

The Kilifi Wind Farm, also known as the Mombasa Cement Wind Power Station, is located near Vipingo on the Kenyan coast (≈3.6° S, 39.9° E) and has an installed capacity of approximately 35 MW (Global Data 2024). At this site, wind variability is likely shaped by coastal–inland pressure gradients and land–sea breeze circulations.

Together, these four wind-farm sites (Lake Turkana, Ngong Hills, Kipeto and Kilifi) span contrasting wind environments, from inland channels to escarpment slopes, plains and coastal settings, and offer a robust basis for evaluating how S2S climate modes modulate wind-power variability across Kenya.

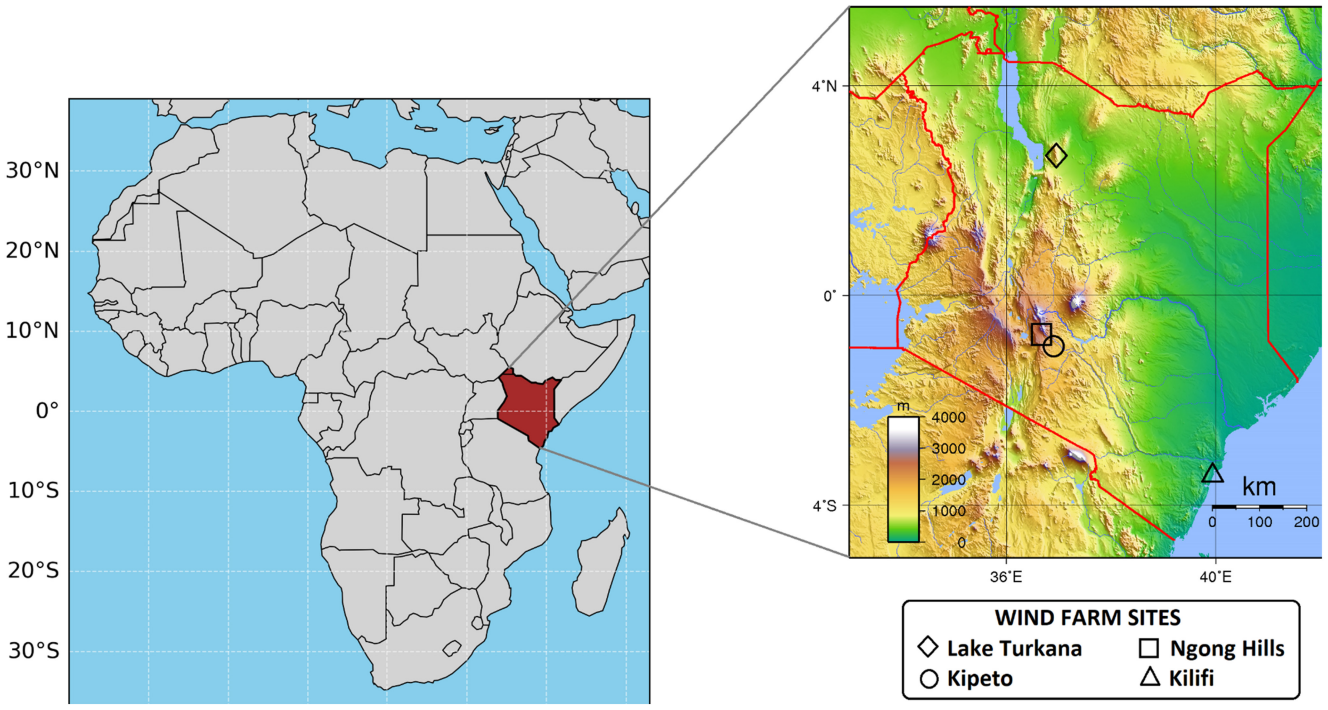


FIGURE 1 | Geographic context of the study domain. Left: Kenya's location within Africa is shown in brown. Right: Topography of Kenya based on a digital elevation model (shaded, in metres above sea level), with red lines delineating the national administrative boundary. The approximate locations of the four wind-farm sites analysed in this study are indicated: Lake Turkana (◇), Ngong Hills (□), Kipeto (○) and Kilifi (△).

14698080, 2026, 4, Downloaded from https://rmets.onlinelibrary.wiley.com/doi/10.1002/met.70221 by NICE, National Institute for Health and Care Excellence, Wiley Online Library on [06/10/2026]. See the Terms and Conditions (https://onlinelibrary.wiley.com/terms-and-conditions) on Wiley Online Library for rules of use; OA articles are governed by the applicable Creative Commons License

2.2 | Data

Building on the description of Kenya's diverse wind environments and the four focal wind-farm sites, this section outlines the reanalysis, observational and climate mode index datasets underpinning our analysis of wind-power variability.

2.2.1 | ERA5 Reanalysis

We use 45 years of ERA5 reanalysis data (1980–2024; Hersbach 2000), produced by the European Centre for Medium-Range Weather Forecasts (ECMWF). ERA5 provides hourly 100 m winds on a 0.25° × 0.25° grid, which we analyse across Kenya. This dataset has been shown to outperform other global reanalyses in capturing observed wind characteristics (Ramon et al. 2019).

2.2.2 | Wind-Farm Observations and Wind-Power Potential Dataset

Observed wind-power generation data were obtained from KenGen for three operational wind farms in Kenya: Lake Turkana and Ngong Hills, both with 50 m turbine hub heights, and Kipeto, with an 80 m hub height. These generation records cover January 2021 to December 2023. No equivalent generation records were available for Kilifi. In this study, the observed generation records are used for site-level analysis at Lake Turkana and Ngong Hills. Kipeto is excluded from the site-level analysis because it is geographically close to Ngong Hills (Figure 1, right subplot) and occupies a similar high-elevation wind regime, but it is retained, together with Kilifi, in the broader spatial analysis of wind-speed variability.

For these two focal sites, we use a daily wind-power potential time series (1980–2024) produced in a companion study (Ang'u et al. 2026), with the key steps relevant to this analysis summarised here for completeness. In that companion modelling study, the wind-power potential dataset was produced from ERA5 100 m wind speeds extracted at the nearest grid point to each wind-farm location. ERA5 100 m winds were used in preference to 10 m winds because they are closer to typical turbine hub heights and are therefore more representative of the flow experienced by wind turbines. In contrast, 10 m winds are more strongly influenced by surface characteristics, including land cover, surface roughness and local terrain effects, and would require a larger vertical adjustment to hub height. Wind speeds were adjusted between heights using a standard vertical wind-profile power law, following common practice in wind-energy studies (e.g., Bloomfield et al. 2019):

$$U_{hub} = U_{100}\left(\frac{z_{hub}}{100}\right)^{\alpha}$$

where U_{100} is the ERA5 wind speed at 100 m, U_{hub} is the wind speed at turbine hub height, z_{hub} is the hub height in metres, and α is the wind-shear exponent, set to 1/7.

Subsequently, the site-specific height adjustment and Weibull Quantile Mapping (WQM; Maciel-Tiburcio et al. 2025) were then applied according to the height of the available wind-speed observations. At Lake Turkana, both ERA5-derived and observed wind-speed time series were available at 100 m, so WQM was applied at 100 m before the corrected winds were scaled to the 50 m hub height. At Ngong Hills, observations were available at 50 m; the ERA5 100 m wind-speed time series was therefore first scaled to 50 m, and WQM was then applied at the observational and hub-height level.

The bias-corrected hub-height winds were then converted to wind-power potential using manufacturer turbine power curves, following common practice in related studies (e.g., Cannon et al. 2015; Bloomfield et al. 2019; Lledó et al. 2019). A wind-speed-dependent dynamic-efficiency adjustment, calibrated from observed generation records, was also applied during the wind-to-power conversion in Ang'u et al. 2026. The resulting time series represents wind-power *potential* rather than realised electricity production, as site-specific operational constraints, including, turbine availability, grid curtailment and maintenance downtime, are not explicitly modelled. Nevertheless, the approach provides a physically based estimate of site-level wind-energy variability suitable for S2S predictability analysis and has been applied in previous European and African wind-energy studies (e.g., Brayshaw et al. 2011; Bloomfield et al. 2019, 2022).

In summary, the companion modelling study of Ang'u et al. (2026) used observed wind-speed records, which are not analysed directly here, to calibrate ERA5-derived winds. Observed generation records were then used to inform the dynamic-efficiency adjustment applied in the wind-to-power conversion. This approach yields a monotonic relationship between wind speed and wind-power potential below turbine cut-out speeds, which are rarely exceeded. Consequently, the relative ranking of low- and high wind-power days is largely preserved. This supports the percentile-based analysis used later in this study and reduces sensitivity to the specific details of the wind-to-power conversion method.

2.2.3 | Climate Mode Indices: MJO, ENSO and IOD

MJO activity is characterised over 1980–2024 using the daily Real-time Multivariate MJO index (RMM; Wheeler and Hendon 2004) from the Australian Bureau of Meteorology, which describes the phase and amplitude of the MJO's eastward-propagating convective envelope across eight canonical phases.

ENSO and IOD are represented using monthly indices from NOAA's Physical Sciences Laboratory over the same 45-year period. ENSO is defined using the Niño 3.4 SST anomaly index from ERSSTv5 (Huang et al. 2017), while the IOD is defined using the Dipole Mode Index (DMI) from HadISST1.1, representing the SST anomaly gradient between the western and southeastern equatorial Indian Ocean (Saji et al. 1999; Rayner et al. 2003).

2.3 | Methods

This section describes the analytical framework used to quantify how the MJO, ENSO and IOD modulate wind-speed anomalies and wind-power potential across Kenya.

14698080, 2026, 4, Downloaded from https://rmets.onlinelibrary.wiley.com/doi/10.1002/met.70221 by NICE, National Institute for Health and Care Excellence, Wiley Online Library on [06/10/2026]. See the Terms and Conditions (https://onlinelibrary.wiley.com/terms-and-conditions) on Wiley Online Library for rules of use; OA articles are governed by the applicable Creative Commons License

2.3.1 | Climate Mode Classification and Wind-Anomaly Composites

Following common practice, only days with an RMM amplitude greater than 1 were retained, corresponding to periods of strong MJO activity e.g., Huang et al. (2026). These days were assigned to one of the eight MJO phases. For compositing, phases with similar circulation characteristics were grouped to improve signal-to-noise and physical interpretation: Phases 2–4, associated with enhanced convection over the Indian Ocean, and Phases 6–8, associated with convection over the western Pacific, were combined, while Phases 1 and 5 were retained separately.

ENSO and IOD events persist for several months and often span calendar years (Saji et al. 1999; Ding and Li 2012). To avoid splitting individual events across January–December years, all analyses used an April–March analysis year, capturing the development, peak and decay phases within one continuous period. Peak ENSO and IOD seasons were defined as the half-year periods with the largest climatological amplitude: October–March for ENSO and June–November for IOD. For each mode, the mean index over its peak season was classified using terciles, following Ficchì et al. (2021). Upper-tercile years were classified as positive phases, lower-tercile years as negative phases and middle-tercile years as neutral. For ENSO, these correspond to El Niño, La Niña and Neutral conditions; for IOD, they correspond to positive, negative and neutral DMI phases. This gives a balanced sample of 15 positive, 15 negative and 15 neutral years for each mode over 1980–2024. The resulting ENSO and IOD year classifications are provided in Table S1.

Daily ERA5 100 m wind-speed anomalies were calculated by subtracting the 1991–2020 daily climatology for each calendar day and smoothed using a 31-day running average to reduce climatic variability as in Masukwedza et al. (2025). Composites were then constructed by calendar month and corresponding climate-mode state: MJO phase or phase group, ENSO category and IOD category. Seasonal composites were also produced for April–May–June (AMJ), July–August–September (JAS), October–November–December (OND) and January–February–March (JFM) using the April–March analysis year. Composite anomalies were expressed as percentage differences from the corresponding seasonal climatological mean wind speed to aid interpretation, particularly where background winds are weak.

Statistical significance was assessed independently at each grid point and season using non-parametric bootstrap resampling. MJO composites were tested against inactive MJO days (RMM amplitude ≤ 1), while ENSO- and IOD-conditioned composites were tested against the full 1980–2024 seasonal climatology. This approach quantifies total modulation relative to the mean seasonal state relevant for wind-energy planning, rather than departures from neutral years only. For each mode–season combination, bootstrap distributions were generated by resampling the relevant reference pool with replacement 10,000 times. Two-sided empirical p values were calculated from the proportion of bootstrap samples with mean anomalies at least as large as the observed composite anomaly. To account for multiple spatial testing, p values were adjusted using the Benjamini–Hochberg false-discovery-rate correction ($\alpha_{FDR} = 0.05$; Wilks 2016) for each mode–season combination.

Together, this framework provides a consistent basis for diagnosing how MJO, ENSO and IOD modulate regional winds and wind-power potential across Kenya.

2.3.2 | Site-Level Climate Mode Modulation of Wind-Power Variability

Site-level analyses were performed for Lake Turkana and Ngong Hills using the wind-power potential dataset described in Section 2.2.2. Daily wind-power potential values were paired with the corresponding daily MJO phase and monthly ENSO/IOD state to assess climate-mode modulation of wind-power variability at each site.

For the MJO analysis, full phase resolution was retained to capture phase-specific modulation of wind-power potential. Percentile-based thresholds were used because they are widely applied in extreme-event and impact analyses (e.g., Yang and Yue 2024; Masukwedza et al. 2025), and provide a practical balance between identifying meaningful departures and retaining sufficient sample sizes for phase-conditioned statistics (Wilks 2019). In this study, low- and high wind-power events are defined using site-specific monthly thresholds calculated from the 1980–2024 modelled wind-power potential climatology. Values below the 25th percentile are classified as low wind-power events, while values above the 75th percentile are classified as high wind-power events. These thresholds represent relative departures from each site's own monthly climatology rather than absolute generation limits. For each month–MJO phase combination, we then use a risk ratio to quantify how the likelihood of these percentile-defined events changes relative to monthly climatology:

$$\text{Risk ratio} = \frac{P(\text{event} \mid m, \varphi)}{P(\text{event} \mid m)}$$

where m is the calendar month, φ is the MJO phase, P (event | m, φ) is the event probability for a given month and MJO phase, and P (event | m) is the corresponding monthly climatological event probability. A risk ratio of 1 indicates no change relative to the monthly climatology; values greater than 1 indicate increased likelihood, and values less than 1 indicate reduced likelihood.

To further assess broader distributional shifts, smoothed cumulative distribution functions (CDFs) of daily wind-power potential were estimated for each season and climate-mode state. The MJO was represented using grouped Phases 2–4 and 6–8, ENSO using El Niño and La Niña conditions and the IOD using positive and negative DMI phases. For each subset, a Gaussian kernel density estimate was first calculated using Scott's rule bandwidth, and the corresponding smoothed CDF was obtained by cumulatively summing and normalising the density. Mode-conditioned CDFs were then compared with the corresponding seasonal climatological CDF. Leftward shifts indicate a greater likelihood of lower wind-power potential output, while rightward shifts indicate a greater likelihood of higher output.

14698080, 2026, 4, Downloaded from https://rmets.onlinelibrary.wiley.com/doi/10.1002/met.70221 by NICE, National Institute for Health and Care Excellence, Wiley Online Library on [06/10/2026]. See the Terms and Conditions (https://onlinelibrary.wiley.com/terms-and-conditions) on Wiley Online Library for rules of use; OA articles are governed by the applicable Creative Commons License

2.3.3 | Perfect-Forecast Framework for Climate Mode Predictability

Perfect-forecast experiments estimate the upper bound of predictability associated with large-scale climate modes by assuming that the relevant mode state is perfectly known. Here, forecasts are derived empirically from historical mode-conditioned wind-power distributions rather than from dynamical models. This provides a physically interpretable benchmark for assessing the potential forecast value of MJO, ENSO and IOD information. In wind-energy applications, such conditioning can reveal systematic shifts in wind-speed or wind-power distributions, including changes in the tails that correspond to low- and high-generation periods relevant for operations and risk management (Brayshaw et al. 2011; Lledó et al. 2020). We therefore use a suite of perfect-forecast experiments to quantify the individual and combined contributions of MJO, ENSO and IOD conditioning to S2S wind-power predictability.

We apply this framework to modelled daily wind-power potential time series for 1980–2024 at Lake Turkana and Ngong Hills, the two sites with observed generation records selected for detailed analysis. For each forecast configuration, historical days with matching conditioning criteria are pooled to form an empirical wind-power distribution. The deterministic forecast is defined as the conditional mean of this distribution, while the probabilistic forecast is represented by the full empirical conditional distribution. The conditioning configurations are:

i. Climatology: month;
ii. Single-mode: month + MJO, month + ENSO, month + IOD;
iii. Joint-mode: month + MJO + ENSO, month + MJO + IOD and month + MJO + ENSO + IOD.

Since the climate modes considered here can co-vary (e.g., Sun et al. 2015), the conditioned responses should not be interpreted as uniquely attributable causal effects of any single mode. We do not attempt to remove mode co-variability because the limited number of independent event years makes such separation statistically unreliable after stratifying by mode state, season and site. Instead, the results are interpreted as total conditioned responses associated with each conditioning configuration.

Incremental skill is assessed using nine forecast-skill contrasts: MJO vs. climatology, ENSO vs. climatology, IOD vs. climatology, MJO + ENSO vs. MJO, MJO + IOD vs. MJO, MJO + ENSO + IOD vs. MJO, MJO + ENSO vs. ENSO, MJO + IOD vs. IOD and MJO + ENSO + IOD vs. climatology. This design quantifies the standalone predictive value of each mode, the added value of ENSO and IOD beyond MJO conditioning, and the overall benefit of joint conditioning on all three modes.

2.3.4 | Verification of Perfect-Forecast Experiments

Perfect-forecast experiments were evaluated using leave-one-out cross-validation to avoid in-sample skill inflation. For each target day, the empirical forecast distribution was constructed from all historical days matching the relevant conditioning criteria, excluding the target day itself. Deterministic and probabilistic forecast scores were then calculated against the corresponding daily modelled wind-power value and averaged by season.

Deterministic forecast accuracy was assessed using the Mean Absolute Error (MAE) between the conditional-mean forecast and the corresponding modelled wind-power potential value on the day of interest. Seasonal MAE, MAE_s, was calculated as follows:

$$\mathrm{MAE}_s = \frac{1}{N_s}\sum_{j=1}^{N_s} |f_{s,j} - o_{s,j}|, \quad s \in \{\mathrm{AMJ}, \mathrm{JAS}, \mathrm{OND}, \mathrm{JFM}\}$$

where N_s is the number of forecast-reference pairs in season, s; $f_{s,j}$ is the deterministic perfect-forecast mean for day j in season s, and $o_{s,j}$ is the corresponding daily modelled wind-power value.

Probabilistic forecast performance was assessed using the Continuous Ranked Probability Score (CRPS; Hersbach 2000), computed from the empirical conditional forecast distribution and averaged by season:

$$\mathrm{CRPS}_s = \frac{1}{N_s}\sum_{j=1}^{N_s}\left[\int_{-\infty}^{\infty}\left[F_{s,j}(X) - 1\left(\mathrm{x} \geq o_{s,j}\right)\right]^2 dX\right], \mathrm{S} \in \{\mathrm{AMJ}, \mathrm{JAS}, \mathrm{OND}, \mathrm{JFM}\}$$

where CRPS_s is the seasonal CRPS; $F_{s,j}$ the predictive cumulative distribution function for day j in season s, and all remaining symbols as defined before.

For each of the nine forecast-skill contrasts described in the preceding section, percentage skill improvement was calculated as follows:

$$\text{Skill improvement}\,(\%) = \frac{S_{\mathrm{ref}} - S_{\mathrm{PF\,exp}}}{S_{\mathrm{ref}}} \times 100$$

where S_{ref} is the MAE or CRPS of the reference configuration, and $S_{PF\,exp}$ is the corresponding score for the perfect-forecast experiment being evaluated. Positive values indicate improved performance relative to the reference configuration, with larger positive values indicating greater error reduction. Values near zero indicate little change, while negative values indicate poorer performance.

2.3.5 | Methodological Workflow Summary

Figure 2 summarises the analytical workflow used in this study. Climate-mode states were first classified for the MJO, ENSO and IOD using the RMM, Niño 3.4 and DMI indices, respectively. These classifications were used to construct mode-conditioned datasets of ERA5 100 m wind-speed anomalies and site-level wind-power potential. The datasets were then analysed using spatial composites, site-level low- and high wind-power diagnostics, distributional analyses and perfect-forecast experiments. Together, these steps link large-scale climate-mode variability to wind-speed modulation, wind-power risk and opportunity

14698080, 2026, 4, Downloaded from https://rmets.onlinelibrary.wiley.com/doi/10.1002/met.70221 by NICE, National Institute for Health and Care Excellence, Wiley Online Library on [06/10/2026]. See the Terms and Conditions (https://onlinelibrary.wiley.com/terms-and-conditions) on Wiley Online Library for rules of use; OA articles are governed by the applicable Creative Commons License

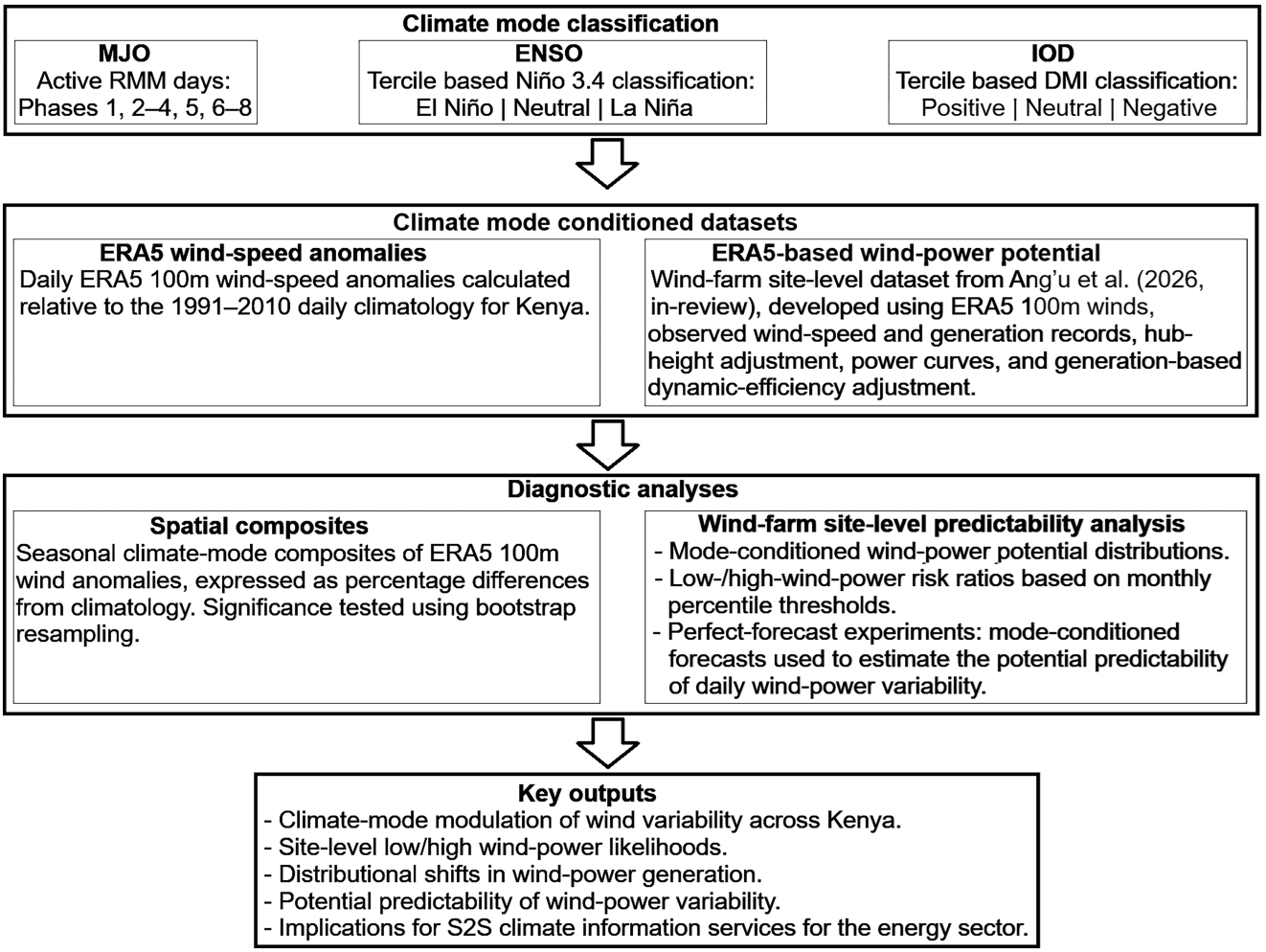


FIGURE 2 | Schematic overview of the methodological workflow used to assess climate-mode modulation and potential predictability of wind-power variability in Kenya.

and potential predictability relevant to S2S climate information services for the energy sector.

3 | Results and Discussion

3.1 | Climatological Wind Regimes and Site-Specific Characteristics

ERA5 100 m winds show strong spatial and seasonal variability across Kenya's wind resource (Figures 3 and 4). A persistent high-wind corridor extends across northern and eastern Kenya, from the Turkana Channel towards the eastern lowlands and coastal regions (Figure 3). This corridor is strongest during May–September, when wind speeds frequently exceed 7–9 ms^{-1} and low-level easterly to southeasterly flow intensifies. Central and western Kenya generally exhibit weaker winds, reflecting complex topography and weaker large-scale pressure gradients.

The site-level cycles reflect this spatial pattern (Figure 4). Lake Turkana lies within the climatological wind maximum and experiences strong, relatively stable winds throughout the year, with monthly mean wind speeds above ~5 ms^{-1} and a peak during August–October, consistent with persistent channelling through the Turkana Channel. Ngong Hills and Kipeto, located near the western escarpment, show stronger seasonal modulation but relatively stable easterly wind directions; wind speeds are weakest during May–July, increase from August and peak around October. Kilifi, on the south-eastern coast, has a distinct seasonal cycle, with wind speeds peaking during May–August above 7 ms^{-1} and weakening during October–March. Its wind direction rotates seasonally, shifting from mainly southerly flow during boreal summer to northeasterly flow during boreal winter, reflecting monsoonal circulation over the western Indian Ocean.

Overall, Figures 3 and 4 show that Kenya's wind-energy resource is shaped by persistent topographic controls, particularly at Lake Turkana, seasonally varying large-scale circulation and contrasts between inland and coastal wind regimes. These patterns are consistent with previous wind-resource assessments for Kenya (e.g., Barasa and Aganda 2016; Kazimierczuk 2019; King et al. 2021). This climatological baseline provides the context for interpreting how S2S climate modes modulate wind speeds and wind-power potential across Kenya and at individual wind-farm sites.

14698080, 2026, 4, Downloaded from https://rmets.onlinelibrary.wiley.com/doi/10.1002/met.70221 by NICE, National Institute for Health and Care Excellence, Wiley Online Library on [06/10/2026]. See the Terms and Conditions (https://onlinelibrary.wiley.com/terms-and-conditions) on Wiley Online Library for rules of use; OA articles are governed by the applicable Creative Commons License

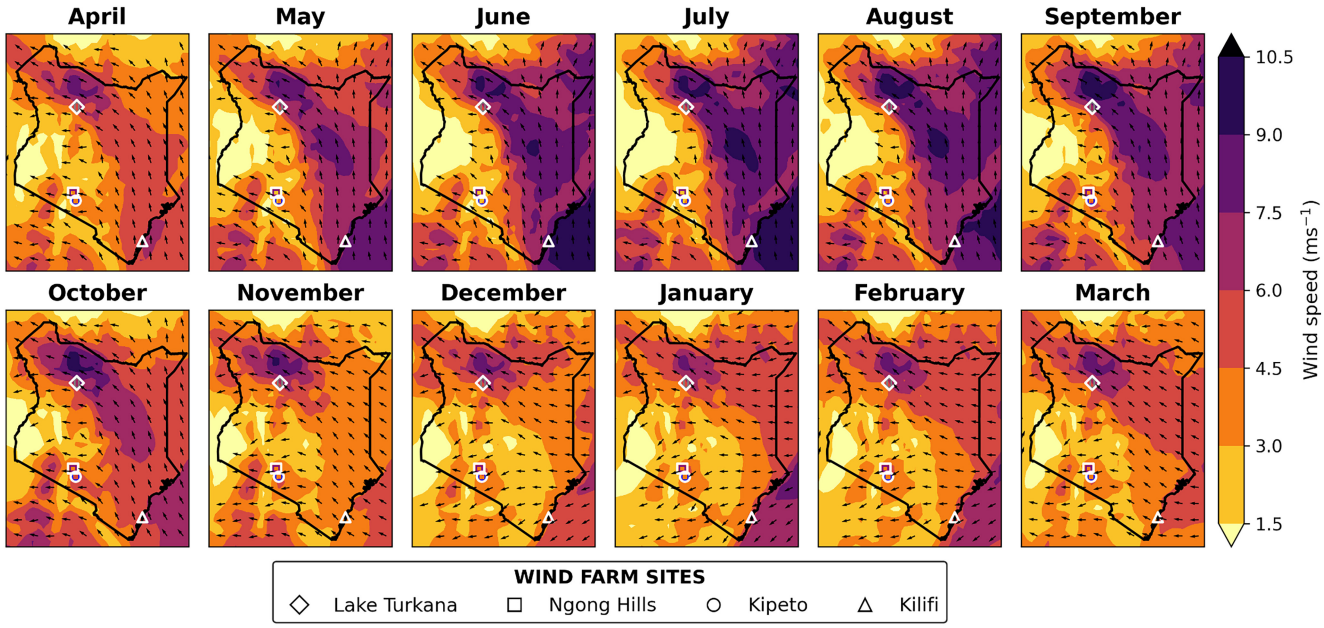


FIGURE 3 | ERA5 100 m monthly wind climatology over Kenya for 1980–2024 (April–March cycle). Colours show monthly mean wind speed (ms^{-1}), and black arrows indicate the mean wind direction, with vectors normalised to unit length. Arrows are only plotted where the mean wind speed exceeds 1.5 ms^{-1}. White markers denote the wind-farm sites: Lake Turkana (◇), Ngong Hills (□), Kipeto (○) and Kilifi (△).

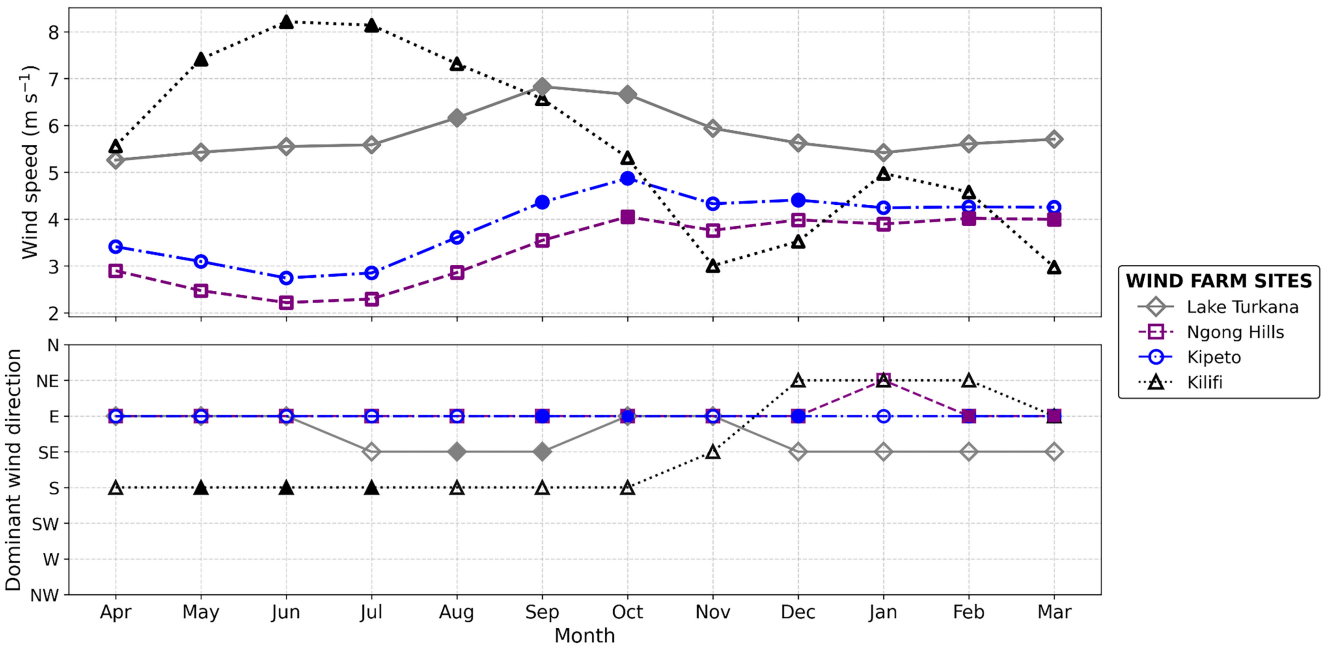


FIGURE 4 | Monthly climatology of wind speed (top) and dominant wind direction (bottom) at the four Kenyan wind-farm sites (Lake Turkana, Ngong Hills, Kipeto and Kilifi), derived from ERA5 100 m winds for 1980–2024. Line colours and marker shapes are consistent across panels. In the upper panel, hollow markers denote monthly mean wind speeds and filled markers identify the three highest-wind months at each site. The lower panel shows the corresponding dominant wind direction; the filled markers indicate the three highest-wind months (as identified in the upper panel), while hollow markers denote all other months.

3.2 | Influence of S2S Climate Modes on Kenyan Wind Variability

This section examines how near-hub-height wind variability is modulated by S2S climate modes across Kenya. Building on the climatological baseline in Section 3.1, we present spatial composites of wind-speed anomalies conditioned on the MJO, ENSO and IOD, following the framework in Section 2.3.1. Results are organised by climate mode to highlight their distinct timescales, spatial signatures and influence on wind-energy-relevant regions.

14690080, 2026, 4, Downloaded from https://rmets.onlinelibrary.wiley.com/doi/10.1002/met.70221 by NICE, National Institute for Health and Care Excellence, Wiley Online Library on [06/10/2026]. See the Terms and Conditions (https://onlinelibrary.wiley.com/terms-and-conditions) on Wiley Online Library for rules of use; OA articles are governed by the applicable Creative Commons License

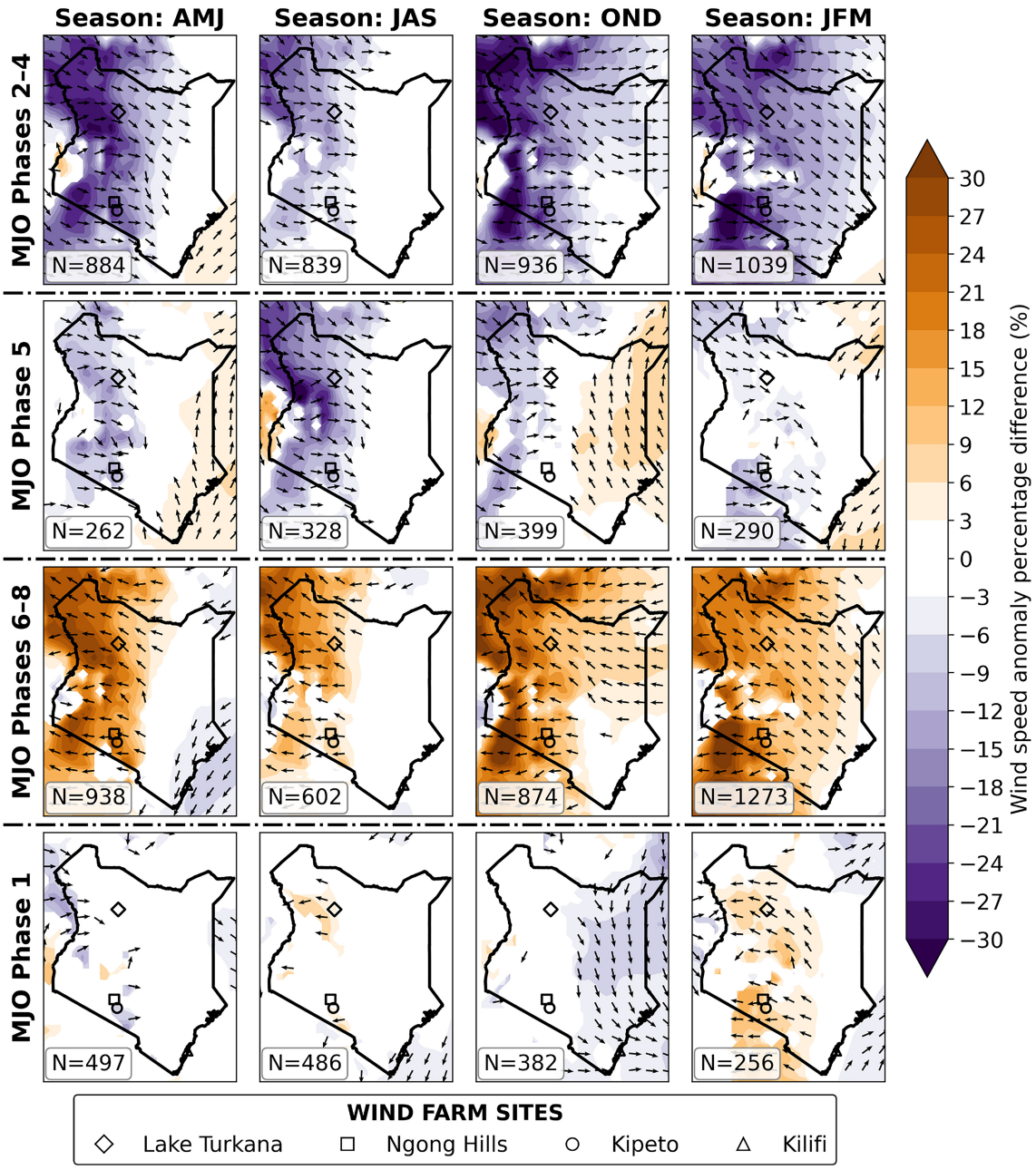


FIGURE 5 | ERA5 100 m wind speed anomalies (1980–2024), composited by grouped MJO phases (rows: Phases 2–4; Phase 5; Phases 6–8; Phase 1) and 3-month seasons (left to right columns: AMJ, JAS, OND and JFM), expressed as percentage differences relative to the corresponding 1980–2024 monthly climatology. The sample size (N = ×) shown in the lower-left corner of each panel indicates the number of daily samples contributing to each composite. Colours show statistically significant wind-speed anomaly percentage differences ($p < 0.05$ and |wind-speed anomaly percentage difference| > 3%) and black arrows show anomalous wind vectors (direction only). Black markers denote the four wind-farm sites in Kenya: Lake Turkana (◇), Ngong Hills (□), Kipeto (○) and Kilifi (△).

3.2.1 | The Role of the MJO

Seasonal composites of ERA5 100 m wind-speed anomalies over Kenya for 1980–2024 were constructed by grouped MJO phase and expressed as percentage differences from the corresponding monthly climatology. These four 3-month seasonal composites summarise the seasonal structure of MJO-related wind anomalies and are shown in Figure 5. For completeness, monthly composites showing their annual evolution are provided in Figures S1–S4.

During MJO Phases 2–4, wind speeds are systematically suppressed across much of Kenya. Negative anomalies extend over northern, central and western regions, including the Lake Turkana corridor, with the most substantial reductions occurring during OND and JFM, when anomaly percentage differences frequently exceed −30%. These suppressed conditions are associated with a weakening of the climatological southeasterly low-level flow, as indicated by the accompanying wind vectors. Given that the regions coincide with Kenya's core wind-energy zones, phases 2–4 represent periods of elevated risk for reduced

14690080, 2026, 4, Downloaded from https://rmets.onlinelibrary.wiley.com/doi/10.1002/met.70221 by NICE, National Institute for Health and Care Excellence, Wiley Online Library on [06/10/2026]. See the Terms and Conditions (https://onlinelibrary.wiley.com/terms-and-conditions) on Wiley Online Library for rules of use; OA articles are governed by the applicable Creative Commons License

wind-power generation on subseasonal timescales, particularly at the inland wind-farm sites, with comparatively weaker impacts at the coastal site (Kilifi).

By contrast, MJO Phases 6–8 are associated with widespread enhancement of wind speeds across Kenya and represent the most dynamically robust MJO signal across all inland wind-farm sites, but again, with comparatively weaker impacts at the coastal site (Kilifi). Positive anomalies are spatially extensive across all seasons and are particularly strong during OND and JFM, when wind speeds increase by 30% over large parts of northern and western Kenya. The prominence of the spatial responses observed in these two seasons are consistent with the primary peak season of MJO activity in boreal winter (approximately December–March), which tends to amplify coherent intraseasonal circulation anomalies and strengthens the wind-speed signals associated with active phases (Zhang and Dong 2004). Across all seasons, the Lake Turkana region, which already exhibits the strongest climatological winds, experiences especially pronounced positive anomalies during these phases, indicating a substantial amplification of wind-energy relevant winds. The wind vectors show a strengthening and increased coherence of the climatological south-easterly flow, consistent with enhanced large-scale pressure gradients during these MJO phases, a pattern observed in MJO-driven modulations of atmospheric circulation over the western Indian Ocean and East Africa (e.g., Finney et al. 2019; Peal and Collier 2025).

Such modulation of regional low-level circulation by the MJO is consistent with known teleconnections impacting East African rainfall and atmospheric dynamics (e.g., Pohl and Camberlin 2006a, 2006b; Nicholson 2017; Peal and Collier 2025). MJO Phase 5 exhibits a transitional, spatially heterogeneous response, with weak negative anomalies over western and central Kenya and positive anomalies over eastern and coastal regions, particularly during OND. Furthermore, Phase 1 shows the weakest and most fragmented anomalies, suggesting limited modulation of Kenya's wind field. Together, Phases 1 and 5 appear to mark transitions between the enhanced-wind regime of Phases 6–8 and the suppressed-wind regime of Phases 2–4.

Overall, Figure 5 shows that the MJO produces a systematic, phase-dependent modulation of Kenya's wind field, superimposed on the seasonal climatology. The suppressed-wind signal during Phases 2–4 and enhanced-wind signal during Phases 6–8 is spatially coherent and robust across seasons.

3.2.2 | The Role of ENSO

Seasonal ERA5 100 m wind-speed anomalies over Kenya for 1980–2024 were composited by ENSO phase across the four 3-month seasons and expressed as percentage differences from the corresponding monthly climatology (Figure 6). Monthly composites showing the annual evolution of these ENSO-related signatures are provided in Figures S5 and S6.

Compared with the more spatially coherent MJO signal shown in Figure 5, ENSO produces a weaker and more seasonally dependent modulation of Kenyan winds as shown in Figure 6. During El Niño, wind-speed anomalies are generally negative in AMJ and OND, with the strongest and most spatially extensive suppression during OND, when negative anomalies extend across much of northern, central and eastern Kenya. This includes the Lake Turkana corridor and inland wind-energy regions, where reduced winds are accompanied by weakened and less coherent low-level flow. In contrast, JAS shows positive anomalies over western and north-western Kenya, extending towards the Lake Turkana corridor, with local increases of around 6%–15%. JFM anomalies are weaker and more spatially fragmented, with only localised signals.

The La Niña response is not a simple sign reversal of El Niño, but also varies strongly by season. During AMJ, wind speeds are enhanced across much of western and north-western Kenya, including the Lake Turkana and Ngong Hills regions, with local positive anomalies exceeding 6%–15%. This is accompanied by more coherent easterly to southeasterly flow, suggesting a strengthening of the background circulation. In JAS, however, La Niña is associated with negative anomalies over western and north–western Kenya, including the Turkana corridor, representing the clearest seasonal contrast with El Niño in the same season. OND shows more localised positive anomalies over parts of northern and eastern Kenya, while JFM remains weak and spatially mixed.

Under ENSO-neutral conditions, anomalies are generally weaker and less spatially coherent than during El Niño or La Niña. However, neutral conditions are not anomaly-free. The clearest signal occurs during OND, when positive wind-speed anomalies extend across parts of northern, western and central Kenya. In AMJ, JAS and JFM, anomalies are smaller and more heterogeneous, indicating that meaningful wind variability persists even in the absence of strong ENSO forcing.

Overall, Figure 6 shows that ENSO modulates Kenyan winds in a seasonally selective and regionally differentiated manner. El Niño is associated with wind suppression most clearly during OND, while La Niña enhances winds most clearly during AMJ and partly during OND. The JAS response shows an opposing ENSO imprint, with El Niño enhancing and La Niña suppressing winds over western and north–western Kenya. These results reinforce that ENSO impacts on Kenya's wind-energy resource depend strongly on season and regional circulation state, and can weaken or reverse sign under different monsoonal backgrounds, consistent with previous evidence for ENSO-related wind-resource variability (Bloomfield et al. 2022; Li et al. 2025).

3.2.3 | The Role of the IOD

Seasonal ERA5 100 m wind-speed anomalies over Kenya for 1980–2024 were composited by IOD phase across the four 3-month seasons and expressed as percentage differences from the corresponding monthly climatology (Figure 7). For completeness, the monthly composites showing the annual evolution of these IOD-related signatures are provided in Figures S7 and S8.

Under positive IOD conditions, anomalies are generally weak and spatially fragmented in AMJ, JAS and JFM, indicating

14698080, 2026, 4, Downloaded from https://rmets.onlinelibrary.wiley.com/doi/10.1002/met.70221 by NICE, National Institute for Health and Care Excellence, Wiley Online Library on [06/10/2026]. See the Terms and Conditions (https://onlinelibrary.wiley.com/terms-and-conditions) on Wiley Online Library for rules of use; OA articles are governed by the applicable Creative Commons License

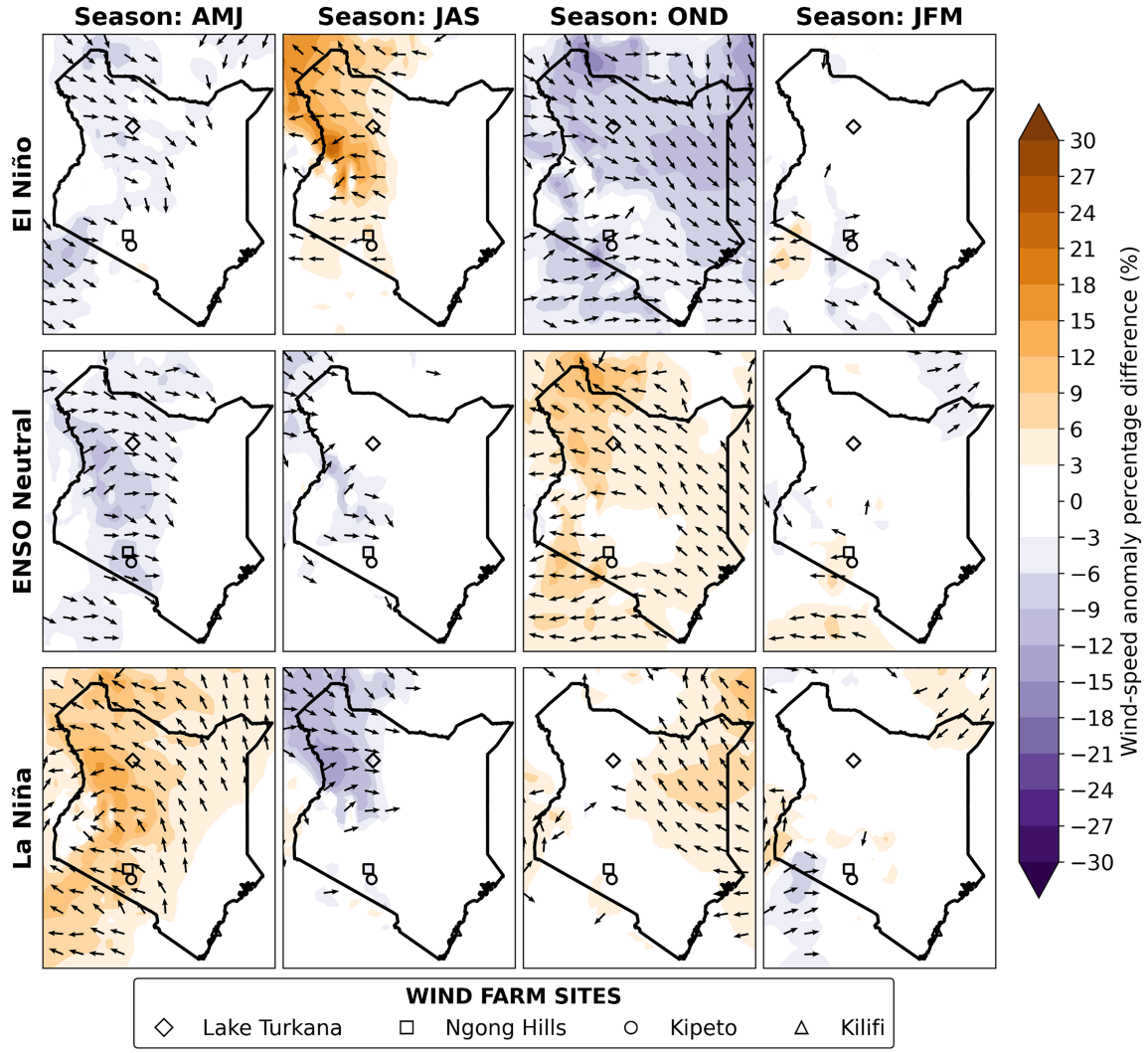


FIGURE 6 | ERA5 100 m wind-speed anomalies over Kenya (1980–2024), composited by ENSO phases (top to bottom rows: El Niño, ENSO Neutral and La Niña) and 3-month seasons (left to right columns: AMJ, JAS, OND and JFM), expressed as percentage differences relative to the corresponding 1980–2024 monthly climatology. Colours show statistically significant wind-speed anomaly percentage differences ($p < 0.05$ and |wind-speed anomaly percentage difference| > 3%), and black arrows show anomalous wind vectors (direction only). Black markers denote the four wind-farm sites in Kenya: Lake Turkana (◇), Ngong Hills (□), Kipeto (○) and Kilifi (△). Sample sizes for each season and ENSO phase composite are $N = 45$ months (≈1350 days).

limited IOD influence outside boreal autumn. By contrast, OND shows the clearest IOD signal, with widespread negative wind-speed anomalies across northern, central and eastern Kenya, including the Lake Turkana corridor and inland wind-energy regions. Local reductions exceed ~9%, and the wind vectors indicate a weakening of the climatological easterly to southeasterly low-level flow. This pattern is consistent with reduced pressure-gradient support for winds along key wind-energy corridors. These ENSO- and IOD-conditioned composites should be interpreted in light of the specific event years sampled in the 1980–2024 record, including the observed co-occurrence of ENSO and IOD states. Since El Niño and positive IOD events often co-occur and strengthen during OND (Shinoda et al. 2004; Shi et al. 2012), and since 9 of 15 El Niño years in our classification coincide with positive IOD years (Table S1), the similarity between the OND ENSO signal in Figure 6 and the IOD signal in Figure 7 is most plausibly interpreted as a combined Indo-Pacific forcing rather than an isolated ENSO or IOD-only response. This is also consistent with the association between positive IOD conditions, enhanced East African short rains and wetter-than-normal regional conditions (Zheng et al. 2025; Palmer et al. 2023), with related circulation and moisture-transport anomalies providing a plausible pathway for co-modulating wind-energy-relevant flow over Kenya (Moihamette et al. 2024).

Under negative IOD conditions, the OND signal largely reverses. Positive wind-speed anomalies extend across much of Kenya, with the strongest enhancements over northern and central regions, including the Turkana corridor, where local increases exceed ~9%. The accompanying vectors indicate stronger and more coherent easterly to southeasterly flow, consistent with enhanced pressure-gradient forcing across the western Indian Ocean–East Africa sector. These patterns align with the regional tendency for drier-than-normal conditions during negative IOD

14690080, 2026, 4, Downloaded from https://rmets.onlinelibrary.wiley.com/doi/10.1002/met.70221 by NICE, National Institute for Health and Care Excellence, Wiley Online Library on [06/10/2026]. See the Terms and Conditions (https://onlinelibrary.wiley.com/terms-and-conditions) on Wiley Online Library for rules of use; OA articles are governed by the applicable Creative Commons License

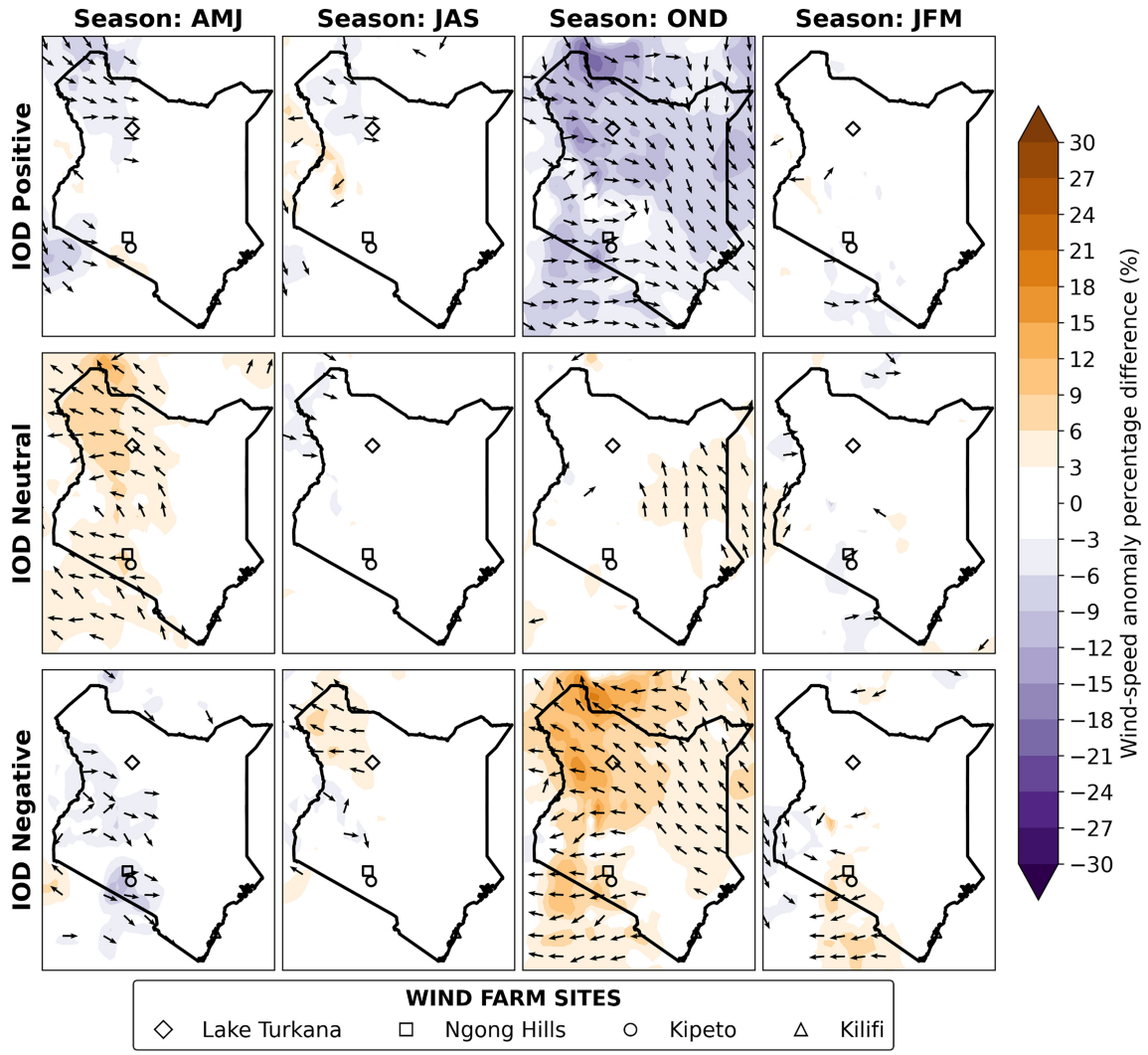


FIGURE 7 | ERA5 100 m wind-speed anomalies over Kenya (1980–2024), composited by IOD phases (top to bottom rows: Positive, Neutral and Negative) and 3-month seasons (left to right columns: AMJ, JAS, OND and JFM), expressed as percentage differences relative to the corresponding 1980–2024 monthly climatology. Colours show statistically significant wind-speed anomaly percentage differences ($p < 0.05$ and |wind-speed anomaly percentage difference| > 2%), and black arrows show anomalous wind vectors (direction only). Black markers denote the four wind-farm sites in Kenya: Lake Turkana (◇), Ngong Hills (□), Kipeto (○) and Kilifi (△). Sample sizes for each season and IOD phase composite are $N = 45$ months (≈1350 days).

events (Zheng et al. 2025). Outside OND, the negative IOD imprint is weaker and less coherent: JAS shows modest positive anomalies over the north-west, AMJ shows localised negative anomalies over western and central Kenya, and JFM remains spatially fragmented. This muted JFM response is consistent with boreal-winter conditions when MJO-driven subseasonal variability is typically strongest (Zhang and Dong 2004), suggesting limited IOD influence on Kenya's wind field in early boreal winter.

Under neutral IOD conditions, anomalies are generally weaker and more spatially variable, but they are not absent. AMJ shows modest positive anomalies over western and north–western Kenya, while JAS and JFM are weak and patchy. In OND, neutral IOD conditions show localised positive anomalies over parts of eastern and central Kenya, but these are weaker and less extensive than the negative-IOD OND signal. These patterns indicate that wind variability persists even without strong IOD forcing, reflecting the influence of other modes and regional circulation variability.

Taken together, these results show a clear hierarchy of climate-mode influences on Kenyan wind variability. The MJO provides the dominant, phase-dependent subseasonal signal across seasons, with robust impacts over inland wind-energy corridors. ENSO exerts a weaker but seasonally selective influence, particularly during JAS and OND, with responses that vary by season and phase. The IOD is more tightly season-locked, with its strongest imprint during OND, when positive IOD weakens and negative IOD strengthens winds across key inland regions. The similarity between positive IOD and El Niño OND patterns suggests coupled Indo-Pacific forcing. Outside OND, IOD effects are comparatively weak, leaving ENSO and especially the MJO as the primary sources of wind variability.

3.3 | Climate-Mode Modulation of Site-Level Wind-Power Potential

Building on the spatial composite results, this section examines how climate-mode signals translate into site-level wind-power

14690080, 2026, 4, Downloaded from https://rmets.onlinelibrary.wiley.com/doi/10.1002/met.70221 by NICE, National Institute for Health and Care Excellence, Wiley Online Library on [06/10/2026]. See the Terms and Conditions (https://onlinelibrary.wiley.com/terms-and-conditions) on Wiley Online Library for rules of use; OA articles are governed by the applicable Creative Commons License

potential at Lake Turkana and Ngong Hills. The analysis first quantifies MJO-related changes in the likelihood of low- and high-wind power potential events, then assesses whether conditioning on the MJO, ENSO and IOD produces broader shifts in the daily wind-power potential distribution.

3.3.1 | MJO Modulation of Low- and High-Wind-Power Likelihood

Using the percentile-based wind-power potential thresholds defined in Section 2.3.2, Figure 8 shows clear MJO-phase modulation of low and high wind-power likelihood at both Lake Turkana and Ngong Hills, with low wind-power risk shown in the top row and high wind-power opportunity shown in the bottom row. These diagnostics should be interpreted as changes in the likelihood of monthly percentile-based low/high wind-power conditions, rather than rare extremes.

For low wind-power risk, MJO Phases 2–4 are generally associated with increased likelihood. Risk ratios often exceed 1.5, meaning that low wind-power conditions are at least 50% more likely than under the monthly climatology. In several months, risk ratios approach or exceed 3, indicating a near-tripling or tripling of low wind-power risk. In contrast, Phases 6–8 are consistently associated with reduced low wind-power risk, with risk ratios frequently below 0.5, meaning that low wind-power conditions are less than half as likely as normal.

The high wind-power opportunity result shows the opposite pattern. MJO Phases 2–4 generally reduce the likelihood of high wind-power conditions, while Phases 6–8 increase it across many months at both sites. This reversal between the low- and high wind-power panels indicates a systematic MJO-related shift in the likelihood of lower- and higher-generation conditions.

The signal is strongest and most coherent at Lake Turkana, where Phases 2–4 produce persistent low wind-power risk and Phases 6–8 produce persistent high wind-power opportunity across much of the year. Ngong Hills shows a broadly similar phase dependence, although the response is more variable across months, consistent with its more complex terrain setting and weaker climatological wind regime. Overall, Figure 8 shows that MJO phase reweights the probability of low- and high wind-power conditions on subseasonal timescales. Phases 2–4 represent windows of elevated low-generation risk, while Phases 6–8 represent windows of enhanced wind-power opportunity. This supports the use of MJO phase information as a source of subseasonal predictability for anticipating wind-power variability relevant to energy operations and planning (e.g., Lledó and Doblas-Reyes 2020).

3.3.2 | MJO-, ENSO- and IOD-Conditioned Shifts in Wind-Power Potential

To assess whether the threshold-based signals reflect broader distributional changes, we examine seasonal CDFs of full daily wind-power potential time series. Figure 9 shows Lake Turkana distributions conditioned on MJO, ENSO and IOD states and compared with the corresponding seasonal climatology.

The MJO is shown to produce the clearest and most consistent distributional shifts across seasons. In AMJ, OND and JFM,

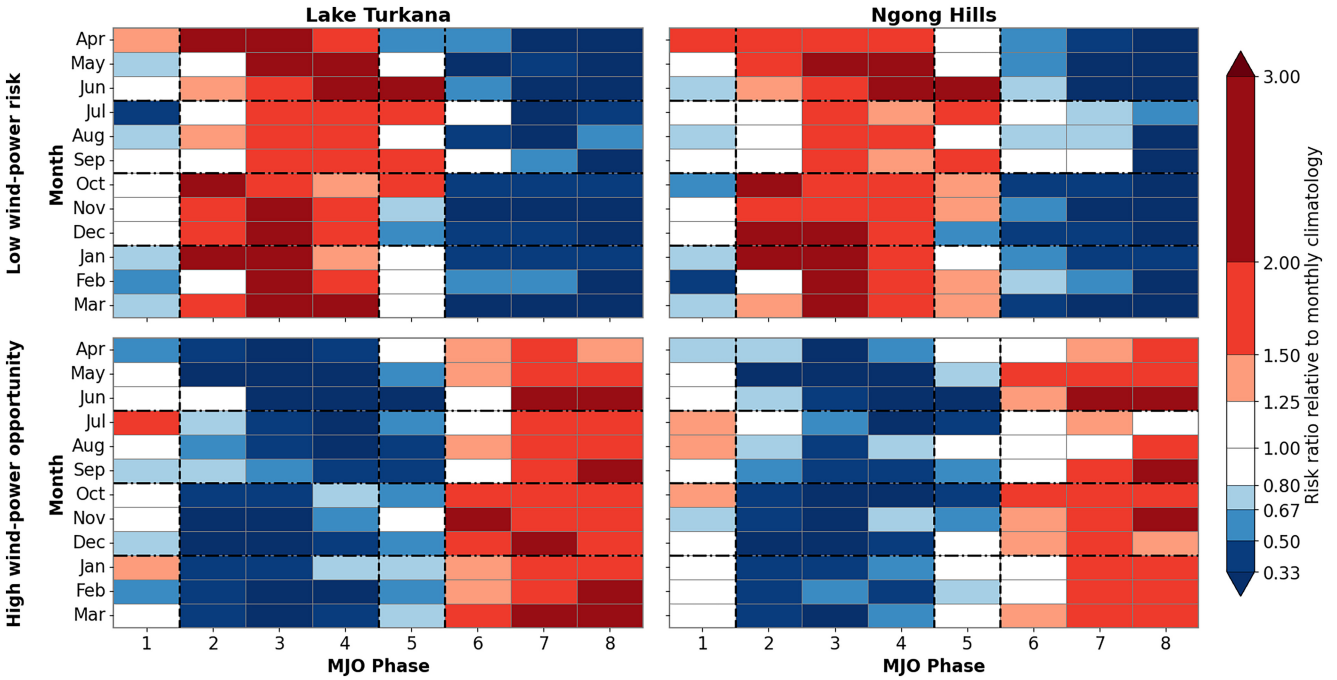


FIGURE 8 | Modulation of low- and high wind-power conditions by MJO phase at Lake Turkana and Ngong Hills. Heatmaps show risk ratios relative to the monthly climatology for daily wind-power values below the site-specific monthly 25th percentile threshold, representing low wind-power risk and above the site-specific monthly 75th percentile threshold, representing high wind-power opportunity. Columns correspond to wind-farm sites: Lake Turkana (left) and Ngong Hills (right). Vertical dashed lines delineate grouped MJO phases: Phase 1, Phases 2–4, Phase 5 and Phases 6–8. Horizontal dash-dotted lines indicate the four 3-month seasons: AMJ, JAS, OND and JFM.

14698080, 2026, 4, Downloaded from https://rmets.onlinelibrary.wiley.com/doi/10.1002/met.70221 by NICE, National Institute for Health and Care Excellence, Wiley Online Library on [06/10/2026]. See the Terms and Conditions (https://onlinelibrary.wiley.com/terms-and-conditions) on Wiley Online Library for rules of use; OA articles are governed by the applicable Creative Commons License

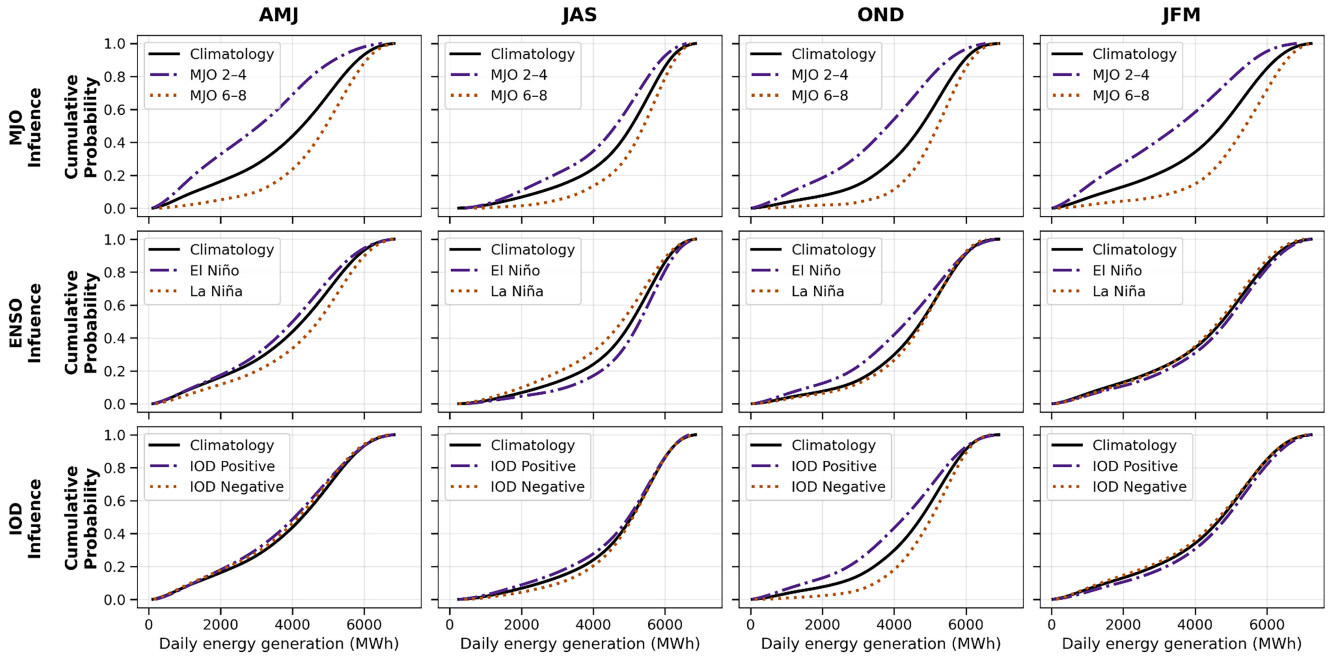


FIGURE 9 | Smoothed empirical CDFs of daily wind-power potential (1980–2024) at Lake Turkana, conditioned on climate modes and season. Results are shown for the MJO (Phases 2–4 and 6–8; top row), ENSO (El Niño and La Niña; middle row) and IOD (positive and negative phases; bottom row) across four seasons (AMJ, JAS, OND, JFM; left to right). The black line denotes the corresponding seasonal climatology.

MJO Phases 2–4 are associated with a marked leftward shift, while Phases 6–8 show a clear rightward shift. This indicates suppressed and enhanced wind-power potential, respectively, across much of the distribution. The MJO signal remains evident in JAS, although the separation from climatology is weaker than in the other seasons.

ENSO produces weaker and more seasonally dependent shifts. In AMJ, El Niño is slightly shifted towards lower wind-power potential, while La Niña is shifted towards higher potential. In JAS, the sign reverses, with El Niño favouring higher potential and La Niña favouring lower potential. OND shows a clearer El Niño-related shift towards lower wind-power potential, while La Niña remains close to or slightly to the right of, climatology. In JFM, ENSO-conditioned distributions remain close to climatology.

The IOD influence is weakest outside OND. In AMJ, JAS and JFM, positive and negative IOD distributions largely follow the climatological distribution. In OND, positive IOD conditions shift the distribution towards lower wind-power potential, while negative IOD conditions shift it towards higher potential, consistent with the spatial wind-anomaly composites in Figure 7.

Similar distributional shifts are also evident at Ngong Hills, with the corresponding results provided in Figure S9. Since these diagnostics are based on modelled wind-power potential rather than realised generation, they should be interpreted as climate-conditioned changes in potential resource availability rather than direct changes in operational power output.

3.4 | Contribution of MJO, ENSO and IOD to Wind-Power Potential Forecast Skill

The preceding results show that MJO, ENSO and IOD signals are expressed in both country-wide wind-speed anomalies and site-level wind-power potential distributions. We next use the perfect-forecast framework described in Section 2.3.3 to quantify their potential contribution to S2S wind-power potential forecast skill.

Perfect-forecast skill improvements at Lake Turkana and Ngong Hills show a clear seasonal and mode-dependent structure (Figure 10). Across both sites and both metrics, MJO conditioning provides the largest single-mode improvement relative to climatology. At Lake Turkana, MJO-only conditioning reduces MAE and CRPS by about 4%–10%, with the largest gains in AMJ, OND and JFM and the weakest gains in JAS. Ngong Hills shows the same seasonal structure, although with slightly smaller gains, with MAE and CRPS reductions generally below 9%. This indicates that MJO phase information improves both deterministic and probabilistic representations of daily wind-power variability.

ENSO- and IOD-only conditioning provide smaller improvements relative to climatology. Their contributions are most evident in OND, where Lake Turkana shows MAE reductions of about 5%, compared with weaker gains at Ngong Hills. Outside OND, ENSO and IOD provide more modest standalone skill, consistent with their weaker and more seasonally constrained wind-speed anomalies shown earlier.

Adding ENSO or IOD to an MJO-conditioned forecast yields secondary improvements. These gains are generally positive but

14698080, 2026, 4, Downloaded from https://rmets.onlinelibrary.wiley.com/doi/10.1002/met.70221 by NICE, National Institute for Health and Care Excellence, Wiley Online Library on [06/10/2026]. See the Terms and Conditions (https://onlinelibrary.wiley.com/terms-and-conditions) on Wiley Online Library for rules of use; OA articles are governed by the applicable Creative Commons License

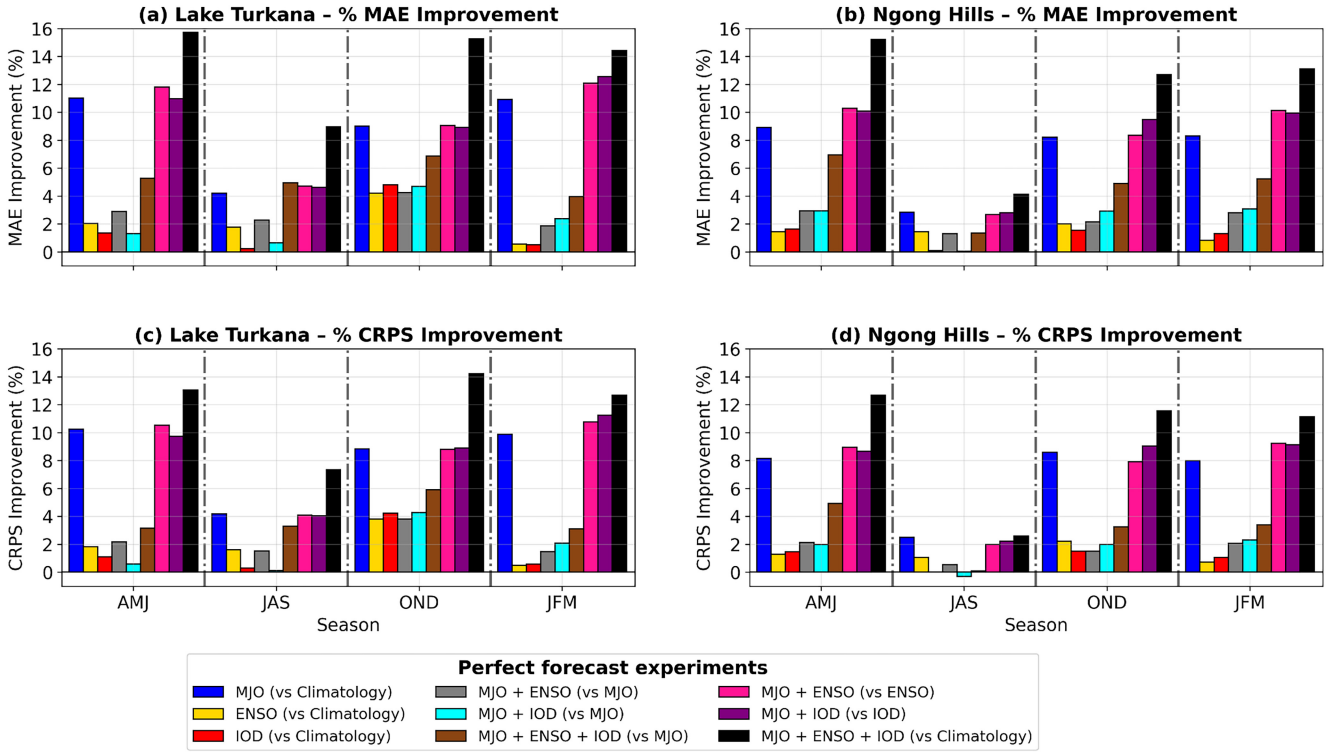


FIGURE 10 | Percent improvement in perfect-forecast skill for daily wind-power potential generation at (a, c) Lake Turkana and (b, d) Ngong Hills, shown by season (AMJ, JAS, OND, JFM). Panels (a, b) report MAE improvements and panels (c, d) report CRPS improvements. Coloured bars denote the set of conditioning experiments: Single-mode relative to seasonal climatology, and incremental gains from adding ENSO and/or IOD to an MJO-conditioned forecast, alongside combined-mode performance relative to climatology, as labelled in the legend.

smaller than the initial gain from MJO conditioning alone, indicating that ENSO and IOD mainly refine an already skillful MJO-conditioned forecast. The added value is strongest when ENSO and IOD are included jointly, with OND reductions reaching about 7% for both MAE and CRPS at Lake Turkana relative to the MJO-only baseline.

The reverse comparisons further emphasise the dominant role of the MJO. Adding MJO to ENSO-only or IOD-only conditioning produces substantially larger improvements than adding ENSO or IOD to MJO, with reductions often approaching or exceeding 10% in AMJ, OND and JFM. This shows that the MJO contains predictive information not captured by the slower interannual modes alone.

Overall, the full MJO + ENSO + IOD configuration relative to climatology yields the largest total skill improvements at both sites, with reductions in MAE and CRPS reaching approximately 16% in the seasons showing the greatest skill gains. Figure 10 therefore reinforces a robust hierarchy of predictability: MJO provides the dominant single-mode contribution; ENSO and IOD provide smaller season-dependent refinements; and combined conditioning on all three modes yields the largest overall improvements as indictated by the largest MAE and CRPS reductions.

4 | Implications for S2S Renewable-Energy Forecasting and Operational Planning in Kenya

The results presented in this study suggest that Kenya's inland wind-power variability contains actionable subseasonal structure that can inform operational "windows of risk and opportunity." In practice, MJO phase information could be used to flag periods when wind-energy generation is more likely to be suppressed, particularly during Phases 2–4, or enhanced, particularly during Phases 6–8. This provides a regime-based planning layer that can complement conventional weather forecasts at lead times where deterministic forecast skill typically declines, consistent with broader evidence that S2S regime and event conditioning can support sector-relevant decision-making, including in energy applications (White et al. 2022).

The MJO provides the primary subseasonal signal for identifying near-term windows of wind-power risk and opportunity. However, these windows occur within a broader seasonal background that is partly shaped by ENSO and the IOD, especially during OND. During this season, El Niño and positive IOD events often co-occur and strengthen the Indo-Pacific influence on East African circulation (Shinoda et al. 2004; Shi et al. 2012). Operational guidance may therefore be more useful when MJO-based subseasonal information is interpreted alongside the prevailing ENSO–IOD state, rather than through ENSO or IOD in isolation.

The larger and more coherent skill gains at Lake Turkana suggest that Kenya's most productive wind-energy corridor may be particularly amenable to S2S guidance. Operationally, this supports prioritising Turkana-focused products: for example, scheduling maintenance during MJO Phases 2–4 where feasible, when generation is more likely to be suppressed, and maximising turbine availability during MJO Phases 6–8,

14698080, 2026, 4, Downloaded from https://rmets.onlinelibrary.wiley.com/doi/10.1002/met.70221 by NICE, National Institute for Health and Care Excellence, Wiley Online Library on [06/10/2026]. See the Terms and Conditions (https://onlinelibrary.wiley.com/terms-and-conditions) on Wiley Online Library for rules of use; OA articles are governed by the applicable Creative Commons License

when enhanced output is more likely. Realising this value will require sustained collaboration among relevant stakeholders in the energy sector.

There is already a foundation for such integration at national and regional levels. KMD routinely monitors large-scale climate modes as part of its forecasting activities: the MJO is considered in extreme rainfall monitoring (Wanjohi 2026), while ENSO and the IOD underpin seasonal climate outlooks used across agriculture, water, health, energy and disaster risk management (Kenya Meteorological Department 2025). At the regional scale, the Intergovernmental Authority on Development (IGAD) Climate Prediction and Applications Centre (ICPAC) also monitors the MJO, ENSO and IOD as part of its climate watch and seasonal forecasting activities for the Greater Horn of Africa (GHA), which includes Kenya (ICPAC 2025). Extending this existing climate-mode monitoring into wind-energy-specific guidance would therefore build on current operational practice rather than require an entirely new forecasting paradigm.

However, several barriers may limit the operational uptake of climate-mode-informed wind-energy services. The predictability identified here is conditional and mode-dependent, so it must be communicated as probabilistic guidance rather than deterministic forecasts. This guidance will only be useful if translated into decision-relevant thresholds, lead times and actions for maintenance scheduling, reserve planning, dispatch decisions or heightened monitoring during periods of increased low- or high-generation risk. Uptake may also be constrained by the limited availability of long, high-quality site-level observations. The short generation records used here limit direct validation of climate-mode-conditioned impacts on realised wind-energy output, particularly for relatively slower varying modes such as ENSO and IOD, which require many years to sample robustly. In addition, the coarse spatial resolution of reanalysis and S2S forecast products may limit their direct use for site-specific operational decisions, particularly in complex terrain where local topography, turbine exposure and channelling effects can strongly shape realised wind conditions. Climate-mode diagnostics are therefore best interpreted as broad regime-based guidance rather than turbine-level forecasts, unless combined with local observations, downscaling or site-specific calibration.

Addressing these barriers will require co-produced S2S wind-energy services designed around operational decisions rather than climate signals alone. Product development should involve forecast producers, energy operators and grid planners in defining useful lead times, forecast update frequency, verification metrics and action thresholds linked to real planning decisions. Testbeds, post-season reviews and event-focused after-action assessments could then be used to refine product formats, evaluate performance and build trust in probabilistic guidance, consistent with established principles for actionable climate information and services (Hirons et al. 2021; Jacob et al. 2025).

Taken together, the results presented in this study support a practical pathway for S2S wind-energy services in Kenya, with potential relevance for wider East Africa: use the MJO as the primary indicator of subseasonal generation risk and opportunity at inland wind-power sites, and use ENSO/IOD as seasonal contexts to sharpen guidance.

5 | Summary and Conclusions

This study assessed how three major climate modes relevant to subseasonal-to-seasonal wind-power variability, the Madden–Julian Oscillation (MJO), El Niño–Southern Oscillation (ENSO) and Indian Ocean Dipole (IOD), modulate wind-speed variability and hence wind-power potential over Kenya. Using ERA5 100 m winds, climate-mode indices, observed wind-power records where available, and modelled daily wind-power potential, we combined spatial composites, site-level diagnostics at Lake Turkana and Ngong Hills and perfect-forecast experiments across four seasons: April–May–June (AMJ), July–August–September (JAS), October–November–December (OND) and January–February–March (JFM).

The results show strong geographical and seasonal contrasts in Kenya's wind resource. A persistent high-wind corridor is centred on northern Kenya and the Turkana Channel, while inland, escarpment and coastal sites exhibit distinct seasonal cycles. This climatological structure provides the baseline for interpreting climate-mode anomalies and predictability.

The MJO emerges as the dominant source of subseasonal wind-power variability. Phases 2–4 are associated with coherent wind suppression across key inland wind-energy regions, while Phases 6–8 favour enhanced winds, especially during OND and JFM. These spatial signals translate into site-level impacts at Lake Turkana and Ngong Hills, where MJO phase changes the likelihood of low- and high-wind-power conditions and shifts the broader daily wind-power potential distribution.

ENSO and IOD provide weaker but physically meaningful seasonal modulation. Their influence is strongest during OND, when positive IOD and El Niño conditions are associated with weakened winds across key inland regions, while negative IOD and La Niña conditions tend to strengthen winds. The similarity between positive IOD and El Niño patterns suggests that coupled Indo-Pacific forcing is important in this season.

Perfect-forecast experiments support this hierarchy of predictability. MJO-only conditioning provides the largest single-mode improvements in deterministic and probabilistic forecast skill at both Lake Turkana and Ngong Hills. ENSO and IOD provide smaller, season-dependent refinements, strongest during OND. Adding ENSO and/or IOD to MJO-conditioned forecasts improves skill modestly, while adding MJO to ENSO- or IOD-only conditioning produces much larger gains. The full MJO + ENSO + IOD configuration gives the largest overall skill improvements, confirming that the MJO carries the dominant predictable subseasonal wind-power signal, with ENSO and IOD acting mainly as seasonal contextual modifiers.

Figure 11 summarises these relationships schematically as a conceptual synthesis rather than a quantitative footprint. It highlights MJO Phases 6–8 as generally favouring enhanced wind-power potential and Phases 2–4 or 2–5 as favouring suppressed potential, particularly over inland wind-energy corridors, with ENSO and IOD providing additional seasonal context during OND.

14690080, 2026, 4, Downloaded from https://rmets.onlinelibrary.wiley.com/doi/10.1002/met.70221 by NICE, National Institute for Health and Care Excellence, Wiley Online Library on [06/10/2026]. See the Terms and Conditions (https://onlinelibrary.wiley.com/terms-and-conditions) on Wiley Online Library for rules of use; OA articles are governed by the applicable Creative Commons License

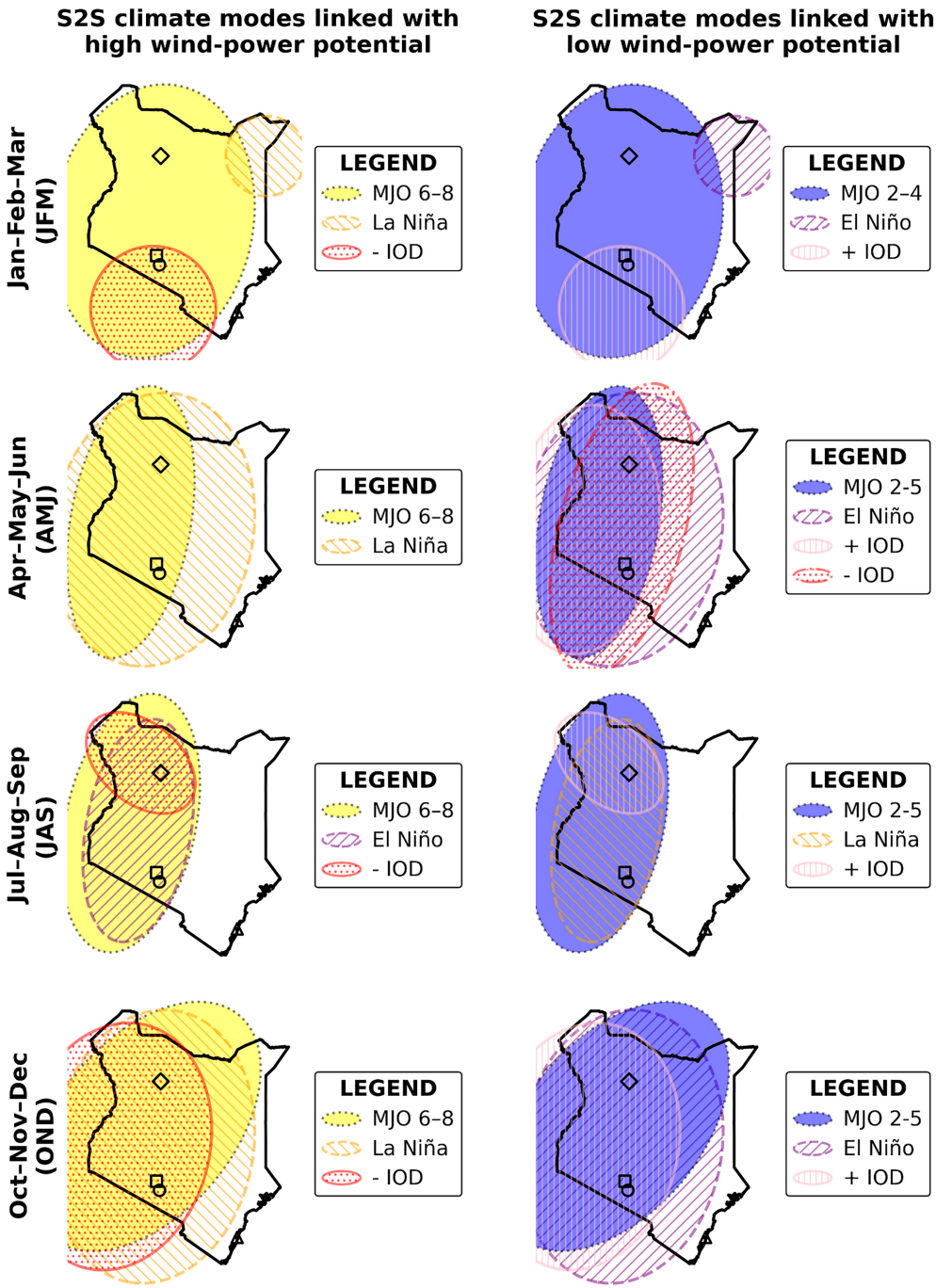


FIGURE 11 | Schematic seasonal summary of S2S climate-mode states associated with higher and lower wind-power potential over Kenya. Rows show the four 3-month seasons (JFM, AMJ, JAS, OND). The left column summarises climate mode states most consistently linked to enhanced wind-power potential, while the right column summarises those linked to suppressed wind-power potential, based on the spatial composites and site-level analyses provided in Sections 3. Coloured ellipses indicate the approximate regions where each driver has its strongest wind-energy-relevant influence. Yellow and blue shading denote MJO phase groupings associated with enhanced winds (Phases 6–8) and suppressed winds (Phases 2–4 or 2–5), respectively. Hatched overlays indicate ENSO phase (El Niño or La Niña), and stippling/striping indicate IOD polarity (+IOD or −IOD), as shown in the legends. Markers show the focal wind-energy sites: Lake Turkana (◇), Ngong Hills (□), Kipeto (○) and Kilifi (△).

These findings provide an evidence base for climate information and services tailored to Kenya's energy sector. The operational implications, including opportunities for KenGen/KMD/ICPAC integration, co-production and barriers to uptake, are discussed in the preceding section.

The Niño 3.4 index used in this study captures broad tropical Pacific basin variability but does not represent the spatial structure of SST anomalies (Abdelkader Di Carlo et al. 2023). Future research could examine whether Kenya's wind-power response varies in response to different ENSO "flavours." Lagged wind responses associated with MJO propagation and the evolution of ENSO and IOD events (Lee et al. 2019; Bi and Yuan 2026) also warrant further investigation particularly because the present study considers only contemporaneous relationships between these climate modes and wind conditions. Finally, the

14690080, 2026, 4, Downloaded from https://rmets.onlinelibrary.wiley.com/doi/10.1002/met.70221 by NICE, National Institute for Health and Care Excellence, Wiley Online Library on [06/10/2026]. See the Terms and Conditions (https://onlinelibrary.wiley.com/terms-and-conditions) on Wiley Online Library for rules of use; OA articles are governed by the applicable Creative Commons License

perfect-forecast experiments presented here estimate potential predictability. A companion follow-on study will assess how much of this potential skill is realised in operational S2S forecast systems and how it can be translated into co-produced climate information services for the energy sector.

Author Contributions

Willis Owino Ochieng: conceptualization, funding acquisition, writing – review and editing, methodology, project administration, supervision, resources. **Gibbon Innocent Tirivanhu Masukwedza:** conceptualization, investigation, writing – original draft, writing – review and editing, visualization, validation, methodology, software, formal analysis, data curation. **Hannah C. Bloomfield:** conceptualization, funding acquisition, methodology, writing – review and editing, project administration, supervision, resources, data curation. **Caroline M. Wainwright:** conceptualization, funding acquisition, methodology, writing – review and editing, supervision, resources, project administration. **Joseph Mutemi:** conceptualization, writing – review and editing, resources, supervision, project administration, methodology, funding acquisition. **Cohen Ang'u:** writing – review and editing, methodology, conceptualization, data curation, formal analysis. **David James Brayshaw:** conceptualization, funding acquisition, methodology, writing – review and editing, project administration, resources, supervision. **Christopher Oludhe:** conceptualization, funding acquisition, supervision, resources, project administration, writing – review and editing, methodology. **Eve de Vincelles:** conceptualization, formal analysis, methodology, writing – review and editing, data curation. **Daniel Olago:** conceptualization, funding acquisition, writing – review and editing, methodology, project administration, supervision, resources. **Wilson Gitau:** conceptualization, funding acquisition, writing – review and editing, methodology, supervision, resources, project administration. **Linda C. Hirons:** conceptualization, investigation, funding acquisition, writing – review and editing, methodology, project administration, supervision, resources. **Steven J. Woolnough:** conceptualization, investigation, funding acquisition, methodology, visualization, writing – review and editing, formal analysis, software, project administration, supervision, resources.

Acknowledgements

We acknowledge the European Centre for Medium-Range Weather Forecasts (ECMWF) and the Copernicus Climate Change Service for access to ERA5 via the Copernicus Climate Data Store. We are grateful to the Kenya Electricity Generating Company (KenGen) for providing site-level operational observations. The opinions and conclusions presented here are those of the authors and do not necessarily represent the positions of the funding bodies or partner institutions. We also thank Eve de Vincelles for conducting the initial exploratory analysis during her placement, which helped shape the early direction of this work. This work used JASMIN, the UK's collaborative data analysis environment (https://jasmin.ac.uk/).

Funding

This work was funded by UK Research and Innovation (UKRI) via the International Science Partnerships Fund (ISPF) (GB-GOV-26-ISPF-STFC-DQ5ZR34-KMC3QB9-2K9RF2Q), through the UKRI469 POWER-Kenya project ('Potential of sub-seasonal Operational Weather and climate information for building Energy Resilience in Kenya'), supported under the OPP680 STFC Africa–UK Physics Partnership collaborative research call. LCH and SJW were also supported by the National Centre for Atmospheric Science through the NERC National Capability International Programme Award (NE/X006263/1).

Conflicts of Interest

The authors declare no conflicts of interest.

Data Availability Statement

ERA5 reanalysis fields were obtained from the Copernicus Climate Data Store and are distributed under the Copernicus Climate Change Service licence. Wind and generation records from the Lake Turkana and Ngong Hills wind farms were supplied by the site operators under data-sharing agreements and cannot be released publicly for confidentiality reasons. Processed/derived datasets that underpin the analyses are available from the corresponding author on reasonable request. Representative scripts used in this study can be provided by the corresponding author upon reasonable request.

References

Abdelkader Di Carlo, I., P. Braconnot, M. Carré, M. Elliot, and O. Marti. 2023. "Different Methods in Assessing El Niño Flavors Lead to Opposite Results." *Geophysical Research Letters* 50, no. 15. https://doi.org/10.1029/2023gl104558.

Afolayan, S., and A. Mekonnen. 2026. "Sub-Seasonal Rainfall Variability and Atmospheric Dynamics During East African Long-Rain." *Atmosphere* 17, no. 1: 85. https://doi.org/10.3390/atmos17010085.

Ang'u, C., H. C. Bloomfield, L. C. Hirons, et al. 2026. "Characterising Wind Power Extremes Over Kenya Using an Enhanced Process-Based Reanalysis-Driven Model." *Renewable Energy* 273: 126048. https://doi.org/10.1016/j.renene.2026.126048.

Barasa, M., and A. Aganda. 2016. "Wind Power Variability of Selected Sites in Kenya and the Impact to System Operating Reserve." *Renewable Energy* 85: 464–471. https://doi.org/10.1016/j.renene.2015.05.042.

Berhane, F., and B. Zaitchik. 2014. "Modulation of Daily Precipitation Over East Africa by the Madden–Julian Oscillation*." *Journal of Climate* 27, no. 15: 6016–6034. https://doi.org/10.1175/jcli-d-13-00693.1.

Berihu, T., W. Chen, and L. Wang. 2026. "The Joint Influence of the Madden Julian Oscillation and Quasi Biennial Oscillation on the Long Rains Over East Africa." *Theoretical and Applied Climatology* 157, no. 4. https://doi.org/10.1007/s00704-026-06128-8.

Bi, Y., and C. Yuan. 2026. "Changes in the Impact of MJO-Induced Oceanic Kelvin Waves on ENSO During 1981–2021." *Atmospheric and Oceanic Science Letters* 100792. https://doi.org/10.1016/j.aosl.2026.100792.

Bloomfield, H. C., D. J. Brayshaw, and A. J. Charlton-Perez. 2019. "Characterizing the Winter Meteorological Drivers of the European Electricity System Using Targeted Circulation Types." *Meteorological Applications* 27, no. 1. https://doi.org/10.1002/met.1858.

Bloomfield, H. C., C. M. Wainwright, and N. Mitchell. 2022. "Characterizing the Variability and Meteorological Drivers of Wind Power and Solar Power Generation Over Africa." *Meteorological Applications* 29, no. 5. https://doi.org/10.1002/met.2093.

Brayshaw, D. J., A. Troccoli, R. Fordham, and J. Methven. 2011. "The Impact of Large Scale Atmospheric Circulation Patterns on Wind Power Generation and Its Potential Predictability: A Case Study Over the UK." *Renewable Energy* 36, no. 8: 2087–2096. https://doi.org/10.1016/j.renene.2011.01.025.

Cannon, D. J., D. J. Brayshaw, J. Methven, P. J. Coker, and D. Lenaghan. 2015. "Using Reanalysis Data to Quantify Extreme Wind Power Generation Statistics: A 33 Year Case Study in Great Britain." *Renewable Energy* 75: 767–778. https://doi.org/10.1016/j.renene.2014.10.024.

Chen, Y., X. Huang, J.-J. Luo, et al. 2023. "Prediction of ENSO Using Multivariable Deep Learning." *Atmospheric and Oceanic Science Letters* 16, no. 4: 100350. https://doi.org/10.1016/j.aosl.2023.100350.

Ding, R., and J. Li. 2012. "Influences of ENSO Teleconnection on the Persistence of Sea Surface Temperature in the Tropical Indian Ocean." *Journal of Climate* 25, no. 23: 8177–8195. https://doi.org/10.1175/jcli-d-11-00739.1.

14698080, 2026, 4, Downloaded from https://rmets.onlinelibrary.wiley.com/doi/10.1002/met.70221 by NICE, National Institute for Health and Care Excellence, Wiley Online Library on [06/10/2026]. See the Terms and Conditions (https://onlinelibrary.wiley.com/terms-and-conditions) on Wiley Online Library for rules of use; OA articles are governed by the applicable Creative Commons License

Fernández, L. 2025. Share of renewables in electricity generation in Kenya 2000-2023. [online] Statista. Accessed Jan 17, 2026. https://www.statista.com/statistics/1276547/share-of-renewables-in-electricity-generation-in-kenya/.

Ficchì, A., H. Cloke, C. Neves, et al. 2021. "Beyond El Niño: Unsung Climate Modes Drive African Floods." *Weather and Climate Extremes* 33: 100345. https://doi.org/10.1016/j.wace.2021.100345.

Finney, D. L., J. H. Marsham, D. P. Walker, et al. 2019. "The Effect of Westerlies on East African Rainfall and the Associated Role of Tropical Cyclones and the Madden–Julian Oscillation." *Quarterly Journal of the Royal Meteorological Society* 146, no. 727: 647–664. https://doi.org/10.1002/qj.3698.

Global Data 2024. Power plant profile: Kilifi Wind Farm, Kenya. [online] Power Technology. Accessed Jan 17, 2026. https://www.power-technology.com/data-insights/power-plant-profile-kilifi-wind-farm-kenya/.

Gudoshava, M., P. Nyinguro, J. Talib, et al. 2024. "Drivers of Sub-Seasonal Extreme Rainfall and Their Representation in ECMWF Forecasts During the Eastern African March-to-May Seasons of 2018–2020." *Meteorological Applications* 31, no. 5. https://doi.org/10.1002/met.70000.

Hashimshony Yaffe, N., and H. Segal-Klein. 2023. "Renewable Energy and the Centralisation of Power. The Case Study of Lake Turkana Wind Power, Kenya." *Political Geography* 102: 102819. https://doi.org/10.1016/j.polgeo.2022.102819.

Hersbach, H. 2000. "Decomposition of the Continuous Ranked Probability Score for Ensemble Prediction Systems." *Weather and Forecasting* 15, no. 5: 559–570. https://doi.org/10.1175/1520-0434(2000)015<0559:dotcrp>2.0.co;2.

Hirons, L., E. Thompson, C. Dione, et al. 2021. "Using Co-Production to Improve the Appropriate Use of Sub-Seasonal Forecasts in Africa." *Climate Services* 23: 100246. https://doi.org/10.1016/j.cliser.2021.100246.

Hirons, L., and A. Turner. 2018. "The Impact of Indian Ocean Mean-State Biases in Climate Models on the Representation of the East African Short Rains." *Journal of Climate* 31, no. 16: 6611–6631. https://doi.org/10.1175/jcli-d-17-0804.1.

Huang, B., P. W. Thorne, V. F. Banzon, et al. 2017. "Extended Reconstructed Sea Surface Temperature, Version 5 (ERSSTv5): Upgrades, Validations, and Intercomparisons." *Journal of Climate* 30, no. 20: 8179–8205. https://doi.org/10.1175/jcli-d-16-0836.1.

Huang, Y., Y. Wei, and H.-L. Ren. 2026. "Modulation of ENSO on the MJO Forecast." *Atmospheric Research* 330: 108510. https://doi.org/10.1016/j.atmosres.2025.108510.

ICPAC. 2025. Pre-GHACOF70 Capacity Building Training Workshop for JJAS 2025 Season, 12–16 May 2025: Workshop report. IGAD Climate Prediction and Applications Centre, Nairobi, Kenya. Accessed May 8, 2026. https://www.icpac.net/documents/1013/PRECOF70_REPORT.pdf.

IRENA. 2025. Renewable capacity statistics 2025. [online] Irena.org. Accessed Jan 17, 2026. https://www.irena.org/Publications/2025/Mar/Renewable-capacity-statistics-2025.

Jacob, D., L. St, A. Clair, et al. 2025. "Co-Production of Climate Services: Challenges and Enablers." *Frontiers in Climate* 7. https://doi.org/10.3389/fclim.2025.1507759.

Kazimierczuk, A. H. 2019. "Wind Energy in Kenya: A Status and Policy Framework Review." *Renewable and Sustainable Energy Reviews* 107: 434–445. https://doi.org/10.1016/j.rser.2018.12.061.

KenGen. 2025. Wind-KenGen-energy for the nation. Accessed July 27, 2026. https://www.kengen.co.ke/our-business/energy-generation/wind/.

Kenya Meteorological Department 2025. Rainfall outlook for the October-November-December (OND) 2025 short-rains season; and review of the June-July-August (JJA) 2025 rainfall season. [online] Kenya Meteorological Department. Accessed May 2, 2026. https://meteo.go.ke/our-products/seasonal-forecast/ond-2025-seasonal-forecast/.

Kilavi, M., D. MacLeod, M. Ambani, et al. 2018. "Extreme Rainfall and Flooding Over Central Kenya Including Nairobi City During the Long-Rains Season 2018: Causes, Predictability, and Potential for Early Warning and Actions." *Atmosphere* 9, no. 12: 472. https://doi.org/10.3390/atmos9120472.

Kim, M., D. Kang, S.-J. Sohn, G. Kim, J. Rhee, and S. Kim. 2025. "Multi-Scale Decomposition for Skillful All-Season MJO Prediction With Deep Learning." *Geophysical Research Letters* 53, no. 1. https://doi.org/10.1029/2025gl117981.

King, J. A., S. Engelstaedter, R. Washington, and C. Munday. 2021. "Variability of the Turkana Low-Level Jet in Reanalysis and Models: Implications for Rainfall." *Journal of Geophysical Research: Atmospheres* 126, no. 10. https://doi.org/10.1029/2020jd034154.

Lee, R. W., S. J. Woolnough, A. J. Charlton-Perez, and F. Vitart. 2019. "ENSO Modulation of MJO Teleconnections to the North Atlantic and Europe." *Geophysical Research Letters* 46, no. 22: 13535–13545. https://doi.org/10.1029/2019gl084683.

Li, Z.-B., M. Sun, C. Shen, and D. Chen. 2025. "ENSO-Driven Seasonal Variability in Near-Surface Wind Speed and Wind Power Potential Across China." *Geophysical Research Letters* 52, no. 9. https://doi.org/10.1029/2025gl115537.

Lledó, L., I. Cionni, V. Torralba, P.-A. Bretonnière, and M. Samsó. 2020. "Seasonal Prediction of Euro-Atlantic Teleconnections From Multiple Systems." *Environmental Research Letters* 15, no. 7: 74009. https://doi.org/10.1088/1748-9326/ab87d2.

Lledó, L., and F. J. Doblas-Reyes. 2020. "Predicting Daily Mean Wind Speed in Europe Weeks Ahead From MJO Status." *Monthly Weather Review* 148, no. 8: 3413–3426. https://doi.org/10.1175/mwr-d-19-0328.1.

Lledó, L., V. Torralba, A. Soret, J. Ramon, and F. J. Doblas-Reyes. 2019. "Seasonal Forecasts of Wind Power Generation." *Renewable Energy* 143: 91–100. https://doi.org/10.1016/j.renene.2019.04.135.

LTWP. 2009. https://www3.dfc.gov/Environment/EIA/laketurkanawind/ESIA%20wind%20farm%20site_2009.pdf.

LTWP. 2019. Accessed Jan 15, 2026. Lake Turkana Wind Power – LTWP. https://ltwp.co.ke/.

Lüdecke, H.-J., G. Müller-Plath, M. G. Wallace, and S. Lüning. 2021. "Decadal and Multidecadal Natural Variability of African Rainfall." *Journal of Hydrology: Regional Studies* 34: 100795. https://doi.org/10.1016/j.ejrh.2021.100795.

Maciel-Tiburcio, A., O. Martínez-Alvarado, and O. Rodríguez-Hernández. 2025. "Evaluating Bias Correction Methods for Wind Power Estimation Using Numerical Meteorological Models." *Renewable Energy* 247: 122927. https://doi.org/10.1016/j.renene.2025.122927.

MacLeod, D. A., R. Dankers, R. Graham, et al. 2021. "Drivers and Subseasonal Predictability of Heavy Rainfall in Equatorial East Africa and Relationship With Flood Risk." *Journal of Hydrometeorology* 22, no. 4: 887–903. https://doi.org/10.1175/jhm-d-20-0211.1.

Masukwedza, G. I. T., V. L. Boult, M. Lazenby, and M. C. Todd. 2025. "Characteristics and Atmospheric Drivers of Large-Scale Agrometeorologically Relevant Dry Spells in Sub-Seasonal to Seasonal Timescales Over Zimbabwe." *Meteorological Applications* 32, no. 2. https://doi.org/10.1002/met.70039.

Maybee, B., N. Ward, L. C. Hirons, and J. H. Marsham. 2022. "Importance of Madden–Julian Oscillation Phase to the Interannual Variability of East African Rainfall." *Atmospheric Science Letters* 24, no. 5. https://doi.org/10.1002/asl.1148.

14698080, 2026, 4, Downloaded from https://rmets.onlinelibrary.wiley.com/doi/10.1002/met.70221 by NICE, National Institute for Health and Care Excellence, Wiley Online Library on [06/10/2026]. See the Terms and Conditions (https://onlinelibrary.wiley.com/terms-and-conditions) on Wiley Online Library for rules of use; OA articles are governed by the applicable Creative Commons License

Mbigi, D., and Z. Xiao. 2021. "Tanzanian Rainfall Responses to El Niño and Positive Indian Ocean Dipole Events During 1951–2015." *Atmospheric and Oceanic Science Letters* 14, no. 6: 100093. https://doi.org/10.1016/j.aosl.2021.100093.

Moihamette, F., W. M. Pokam, I. Diallo, and R. Washington. 2024. "Response of Regional Circulation Features to the Indian Ocean Dipole and Influence on Central Africa Climate." *Climate Dynamics* 62, no. 6: 1–21. https://doi.org/10.1007/s00382-024-07251-w.

Mwangi, E., D. MacLeod, D. Kniveton, and M. C. Todd. 2024. "Variability of Rainy Season Onsets Over East Africa." *International Journal of Climatology* 44, no. 10: 3357–3379. https://doi.org/10.1002/joc.8528.

Nicholson, S. 2015. "The Turkana Low-Level Jet: Mean Climatology and Association With Regional Aridity." *International Journal of Climatology* 36, no. 6: 2598–2614. https://doi.org/10.1002/joc.4515.

Nicholson, S. E. 2017. "Climate and Climatic Variability of Rainfall Over Eastern Africa." *Reviews of Geophysics* 55, no. 3: 590–635. https://doi.org/10.1002/2016rg000544.

Ochieng, P. O., I. Nyandega, B. Wambua, and V. Ongoma. 2022. "Linkages Between Madden–Julian Oscillation and Drought Events Over Kenya." *Meteorology and Atmospheric Physics* 135, no. 1. https://doi.org/10.1007/s00703-022-00948-9.

Palmer, P. I., C. M. Wainwright, B. Dong, et al. 2023. "Drivers and Impacts of Eastern African Rainfall Variability." *Nature Reviews Earth & Environment* 4, no. 4: 254–270. https://doi.org/10.1038/s43017-023-00397-x.

Peal, R., and E. Collier. 2025. "Drivers and Impacts of Westerly Moisture Transport Events in East Africa." *Weather and Climate Dynamics* 6, no. 4: 1365–1378. https://doi.org/10.5194/wcd-6-1365-2025.

Pohl, B., and P. Camberlin. 2006a. "Influence of the Madden–Julian Oscillation on East African Rainfall I: Intraseasonal Variability and Regional Dependency." *Quarterly Journal of the Royal Meteorological Society* 132, no. 621: 2521–2539. https://doi.org/10.1256/qj.05.104.

Pohl, B., and P. Camberlin. 2006b. "Influence of the Madden–Julian Oscillation on East African Rainfall: II. March–May Season Extremes and Interannual Variability." *Quarterly Journal of the Royal Meteorological Society* 132, no. 621: 2541–2558. https://doi.org/10.1256/qj.05.223.

Pohl, B., P. Camberlin, and P. Roucou. 2005. "Typology of Pentad Circulation Anomalies Over the Eastern Africa-Western Indian Ocean Region, and Their Relationship With Rainfall." *Climate Research* 29: 111–127. https://doi.org/10.3354/cr029111.

Ramon, J., L. Lledó, V. Torralba, A. Soret, and F. J. Doblas-Reyes. 2019. "What Global Reanalysis Best Represents Near-Surface Winds?" *Quarterly Journal of the Royal Meteorological Society* 145, no. 724: 3236–3251. https://doi.org/10.1002/qj.3616.

Ratnam, J. V., S. K. Behera, M. Nonaka, and K. R. Patil. 2025. "Skillful Prediction of Indian Ocean Dipole Index Using Machine Learning Models." *Applied Computing and Geosciences* 25: 100228. https://doi.org/10.1016/j.acags.2025.100228.

Rayner, N. A., D. E. Parker, E. B. Horton, et al. 2003. "Global Analyses of Sea Surface Temperature, Sea Ice, and Night Marine Air Temperature Since the Late Nineteenth Century." *Journal of Geophysical Research: Atmospheres* 108, no. D14. https://doi.org/10.1029/2002jd002670.

Rotich, I. K., H. Chepkirui, and P. K. Musyimi. 2024. "Renewable Energy Status and Uptake in Kenya." *Energy Strategy Reviews* 54: 101453. https://doi.org/10.1016/j.esr.2024.101453.

Roy, I., and A. Troccoli. 2024. "Identifying Important Drivers of East African October to December Rainfall Season." *Science of the Total Environment* 914: 169615. https://doi.org/10.1016/j.scitotenv.2023.169615.

Saadi, N., A. Miketa, and M. Howells. 2015. "African Clean Energy Corridor: Regional Integration to Promote Renewable Energy Fueled Growth." *Energy Research & Social Science* 5: 130–132. https://doi.org/10.1016/j.erss.2014.12.020.

Saji, N. H., B. N. Goswami, P. N. Vinayachandran, and T. Yamagata. 1999. "A Dipole Mode in the Tropical Indian Ocean." *Nature* 401, no. 6751: 360–363. https://doi.org/10.1038/43854.

Shi, L., H. H. Hendon, O. Alves, J.-J. Luo, M. Balmaseda, and D. Anderson. 2012. "How Predictable Is the Indian Ocean Dipole?" *Monthly Weather Review* 140, no. 12: 3867–3884. https://doi.org/10.1175/mwr-d-12-00001.1.

Shinoda, T., H. H. Hendon, and M. A. Alexander. 2004. "Surface and Subsurface Dipole Variability in the Indian Ocean and Its Relation With ENSO." *Deep Sea Research Part I: Oceanographic Research Papers* 51, no. 5: 619–635. https://doi.org/10.1016/j.dsr.2004.01.005.

Sun, S., Y. Fang, Y. Zu, L. Liu, and K. Li. 2022. "Increased Occurrences of Early Indian Ocean Dipole Under Global Warming." *Science Advances* 8, no. 47. https://doi.org/10.1126/sciadv.add6025.

Sun, S., J. Lan, Y. Fang, Tana, and X. Gao. 2015. "A Triggering Mechanism for the Indian Ocean Dipoles Independent of ENSO." *Journal of Climate* 28, no. 13: 5063–5076. https://doi.org/10.1175/jcli-d-14-00580.1.

Talib, J., C. M. Taylor, B. L. Harris, and C. M. Wainwright. 2023. "Surface-Driven Amplification of Madden–Julian Oscillation Circulation Anomalies Across East Africa and Its Influence on the Turkana Jet." *Quarterly Journal of the Royal Meteorological Society* 149, no. 754: 1890–1912. https://doi.org/10.1002/qj.4487.

The Wind Power. 2025. Kipeto (kenya)-wind farms-online access-the wind power. Accessed July 27, 2026. https://www.thewindpower.net/windfarm_en_30989_kipeto.php.

UNDP. 2025. Sustainable development goals. [online] United Nations Development Programme. Accessed Jan 17, 2026. https://www.undp.org/sustainable-development-goals.

Vashisht, A., and B. Zaitchik. 2022. "Modulation of East African Boreal Fall Rainfall: Combined Effects of the Madden–Julian Oscillation (MJO) and El Niño–Southern Oscillation (ENSO)." *Journal of Climate* 35, no. 6: 2019–2034. https://doi.org/10.1175/jcli-d-21-0583.1.

Vitart, F., and A. W. Robertson. 2018. "The Sub-Seasonal to Seasonal Prediction Project (S2S) and the Prediction of Extreme Events. Npj Climate and Atmospheric." *Science* 1, no. 1. https://doi.org/10.1038/s41612-018-0013-0.

Wang, J., D. I. V. Domeisen, C. I. Garfinkel, et al. 2025. "The Potential Impacts of Improved MJO Prediction on the Prediction of MJO Teleconnections in the UFS Global Fully Coupled Model." *Climate Dynamics* 63, no. 8. https://doi.org/10.1007/s00382-025-07783-9.

Wanjohi, M. 2026. Kenya Met Predicts When Heavy Rains Will Subside in May Weather Outlook. [online] The Kenya Times ~ Trending, Breaking News and Videos. Accessed May 2, 2026. https://thekenyatimes.com/weather/kenya-met-predicts-when-heavy-rains-will-subside-in-may-weather-outlook/.

Wheeler, M. C., and H. H. Hendon. 2004. "An All-Season Real-Time Multivariate MJO Index: Development of an Index for Monitoring and Prediction." *Monthly Weather Review* 132, no. 8: 1917–1932. https://doi.org/10.1175/1520-0493(2004)132<1917:aarmmi>2.0.co;2.

White, C. J., D. I. V. Domeisen, N. Acharya, et al. 2022. "Advances in the Application and Utility of Subseasonal-To-Seasonal Predictions." *Bulletin of the American Meteorological Society* 103, no. 6: E1448–E1472. https://doi.org/10.1175/bams-d-20-0224.1.

Wilks, D. S. 2016. ""The Stippling Shows Statistically Significant Grid Points": How Research Results Are Routinely Overstated and Overinterpreted, and What to Do About It." *Bulletin of the American*

14698080, 2026, 4, Downloaded from https://rmets.onlinelibrary.wiley.com/doi/10.1002/met.70221 by NICE, National Institute for Health and Care Excellence, Wiley Online Library on [06/10/2026]. See the Terms and Conditions (https://onlinelibrary.wiley.com/terms-and-conditions) on Wiley Online Library for rules of use; OA articles are governed by the applicable Creative Commons License

Meteorological Society 97, no. 12: 2263–2273. https://doi.org/10.1175/bams-d-15-00267.1.

Wilks, D. S. 2019. *Statistical Methods in the Atmospheric Sciences*. Elsevier.

Yang, Y., and T. Yue. 2024. "Variations of Global Compound Temperature and Precipitation Events and Associated Population Exposure Projected by the CMIP6 Multi-Model Ensemble." *Sustainability* 16, no. 12: 5007. https://doi.org/10.3390/su16125007.

Yao, S.-L., R. Wu, P. Lin, P.-S. Chu, H. Tang, and P. Wang. 2026. "Inter-Tropical African Precipitation Regime Shifts Dominated by Tropical Easterly Jet." *Npj Climate and Atmospheric Science* 9, no. 1. https://doi.org/10.1038/s41612-025-01312-5.

Zaitchik, B. F. 2017. "Madden-Julian Oscillation Impacts on Tropical African Precipitation." *Atmospheric Research* 184: 88–102. https://doi.org/10.1016/j.atmosres.2016.10.002.

Zhang, C., and M. Dong. 2004. "Seasonality in the Madden–Julian Oscillation." *Journal of Climate* 17, no. 16: 3169–3180. https://doi.org/10.1175/1520-0442(2004)017<3169:sitmo>2.0.co;2.

Zheng, Y., C.-Y. Tam, and M. Collins. 2025. "Indian Ocean Dipole Impacts on Eastern African Short Rains Across Observations, Historical Simulations and Future Projections." *Earth's Future* 13, no. 6. https://doi.org/10.1029/2024ef005219.

Supporting Information

Additional supporting information can be found online in the Supporting Information section. **Table S1:** ENSO–IOD year classification (1980–2024) used to define composite subsets. Years are grouped by ENSO phase (El Niño, neutral, La Niña) and IOD phase (positive, neutral, negative); the number of years in each bin is shown, along with the corresponding year lists for reproducibility. **Figure S1:** Monthly composites of ERA5 100 m wind anomalies conditioned on MJO phases 1–4 (columns, left to right) for April–September (rows, top to bottom). Shading indicates the wind-speed percentage-difference anomaly (%), and arrows show the corresponding anomalous 100-m wind vectors. N in each panel denotes the number of daily samples contributing to the composite. Purple markers indicate wind-farm sites: Lake Turkana (◇), Ngong Hills (□), Kipeto (○) and Kilifi (△). **Figure S2:** Same as Figure S1, but for October–March (rows, top to bottom) and MJO Phases 1–4 (columns, left to right). **Figure S3:** Same as Figure S1, but for April–September (rows, top to bottom) and MJO Phases 5–8 (columns, left to right). **Figure S4:** Same as Figure S1, but for October–March (rows, top to bottom) and MJO Phases 5–8 (columns, left to right). **Figure S5:** Monthly composites of ERA5 100 m wind anomalies conditioned on ENSO phases: El Niño, Neutral, La Niña (rows, top to bottom) for April–September (columns, left to right). Shading indicates the wind-speed percentage-difference anomaly (%), and arrows show the corresponding anomalous 100-m wind vectors. Purple markers indicate wind-farm sites: Lake Turkana (◇), Ngong Hills (□), Kipeto (○) and Kilifi (△). **Figure S6:** Same as Figure S5, but for October–March (columns, left to right) and ENSO phases: El Niño, Neutral, La Niña (rows, top to bottom). **Figure S7:** Monthly composites of ERA5 100 m wind anomalies conditioned on IOD phases: positive, neutral, negative (rows, top to bottom) for April–September (columns, left to right). Shading indicates the wind-speed percentage-difference anomaly (%) and arrows show the corresponding anomalous 100-m wind vectors. Purple markers indicate wind-farm sites: Lake Turkana (◇), Ngong Hills (□), Kipeto (○) and Kilifi (△). **Figure S8:** Same as Figure S7, but for October–March (columns, left to right) and IOD phases: positive, neutral, negative (rows, top to bottom). **Figure S9:** Smoothed empirical cumulative distribution functions (CDFs) of daily wind-power generation at Ngong Hills, conditioned on climate modes and season. Results are shown for the MJO (Phases 2–4 and 6–8; top row), ENSO (El Niño and La Niña; middle row) and IOD (positive and negative phases; bottom row) across four seasons (AMJ, JAS, OND, JFM; left to right). The black line denotes the corresponding seasonal climatology.

14690080, 2026, 4, Downloaded from https://rmets.onlinelibrary.wiley.com/doi/10.1002/met.70221 by NICE, National Institute for Health and Care Excellence, Wiley Online Library on [06/10/2026]. See the Terms and Conditions (https://onlinelibrary.wiley.com/terms-and-conditions) on Wiley Online Library for rules of use; OA articles are governed by the applicable Creative Commons License